Ambient Noise Cross-Correlation and Surface Wave Dispersion of South India Region

Thesis submitted in partial ful llment of the requirements for the
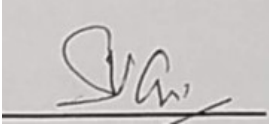BS-MS Dual Degree Programme to

IISER PUNE

Indian Institute of Science Education and Research, Pune

by
Ingale Vaibhav Vijay
20141136

under the guidance of
Prof Shyam S Rai
Professor, Earth and Climate Science Department
IISER Pune

Certificate

This is to certify that this dissertation entitled 1D Inversion of surface wave dispersion for shallow crustal structure of South India towards the partial ful lment of the BSMS Dual Degree Programme at the Indian Institute of Science Education and Research, Pune represents study/work carried out by Ingale Vaibhav Vijay, (Reg. No. : 20141136) at IISER Pune under the super-vision of Prof. Shyam S Rai, Professor, Department of Earth and Climate Sciences, IISER Pune during academic year 2018-2019.

Prof. Shyam S Rai
(Supervisor)

Ingale Vaibhav Vijay
(BSMS Student)

Declaration

I hereby declare that the research work presented in this thesis entitled 1D Inversion of surface wave dispersion for shallow crustal structure of South India submitted by me to the Indian Institute of Science Education and Research, Pune for the award of the degree of BSMS is a bona de record of research work carried out by me. The contents of this thesis, in full or in parts, have not been submitted to any other Institute or University for the award of any degree.

The literature related to the problem investigated has been cited. Due acknowledgements have been made whenever necessary.

Date: September 25, 2019
Place: IISER Pune

Ingale Vaibhav Vijay
BSMS Student

Acknowledgments

Abstract

The peninsular part of the Indian continent (South India) is an important region because of the presence of various geological units. This thesis work focuses on implementing seismic interferometric techniques to ambient seismic noise recorded using broadband seismometers along the East-West profile of South India.

Similar to optical interferometry, seismic interferometry (SI) gives us the detailed interior structure of the Earth by analysing the interference pattern of seismic waves. These interference patterns are obtained using the cross-correlation of seismic traces with one another. The seismic interferometric study helps to obtain the tomographic image of the Earth. This will reconstruct the image of velocity variation in the region of interest. The SI is a vital method for understanding the seismically quiet areas. With the help of this method, one can extract Green's function from ambient noise recorded on the Earth's surface, then the group or phase velocity computation and at last, the tomographic imaging. The tomographic imaging involves producing the phase and group velocity maps. In our work, we obtained the velocity maps for a period range between 3 sec and 15 sec, the group velocity varied from 2.99 km/s to 3.15 km/s and phase velocity varied from 2.9 km/s to 3.15 km/s. But this period range and less variation in group/phase velocity were unable to produce high resolution tomographic image of the region of interest.

Keywords: Ambient Noise, Seismic Interferometry, Green's Function, Group and Phase Velocity, Fast Marching Method, Tomography, Inversion

Contents

List of Figures

1   Introduction

Interferometry is a technique in which propagating waves are superposed to extract the information about a medium. Fields like astronomy, fiber optics, oceanography, seismology and remote sensing evolved to investigate the medium properties with the use of interferometry. This interferometry term tells about the interaction between pairs of the signal so to obtain the enlightenment about the object under study from the difference of those signals. While studying optical properties of a particular medium, we use the energy but not the phase which leads to loose some information about the medium. Hence, to analyze the phase, we use interference between two optical signals or waves with different optical length [Michelson and Morley, 1887]. To understand the optical properties of the medium, scientists and engineers are using interferometry for more than centuries.

Similar to optics, in seismology, we use interferometry to investigate the sub-surface properties of the earth. Unlike the optical interferometry, we have access to phase in seismic interferometry, but for better imaging of the earth, we require regular and dense source distribution. The regularity of sources depend on the geometry of earthquake locations and corresponding recording stations. Also, due to irregular and relatively large distance between the earthquake source and recording station, high frequencies will be lacking from the waveform because of attenuation and scattering over the distance. This will create the problem in imaging of shallow crustal structure as it uses the high frequency information from the waveform. So on the demand of dense sources in global scale motivated scientists to bring up the seismic interferometry into the light.

1.1   Seismic Interferometry using Ambient Noise

Claerbout [1968] introduced the use of noise in seismic by acquiring the reflection response from a one-dimensional correlation of the transmission waves. During this period, one conjecture was emerged saying that: "the cross-correlation of noise recorded at two different locations of receivers in three-dimensional heterogeneous medium gives a response that would be observed at one of the locations if there was a source at the other." Duvall Jr et al. [1993] demonstrated this method of creating artificial source using the helioseismological data and Lobkis and Weaver [2001] demonstrated using ultrasound waves based on normal mode expansion.

The technique of converting ambient noise into a deterministic signal to obtain the sub-surface structure is referred to as passive seismic interferometry [Curtis et al., 2006, Wapenaar et al., 2010a,b]. The first study was done by Campillo and Paul [2003] for creating impulse response using coda waves. The seismic noise correlations were used for the first time in 2005 in California [Shapiro et al., 2005]. The method provided higher spatial accuracy than for conventional techniques. After that, the popularity of this method increased with the development and application to many geological objects. The main advantages of this method over the traditional approaches are: no requirement of artificial source, uniformity and dense illumination of the region of interest, useful in the regions where no earthquakes are recorded.

Extracting the surface wave empirical Green's Functions (GF) using ambient seismic noise and inferring the Rayleigh [Shapiro et al., 2004, Sabra et al., 2005b] and Love waves [Lin et al., 2008, Xie et al., 2015] group and phase velocities is well studied. The study of surface waves using cross-correlations obtained from ambient noise is well established because they are dominated in the GF between two stations on the Earth. Also, the interactions of ocean and atmosphere with the Earth's surface generate the ambient noise sources [Longuet-Higgins, 1962]. With the help of conventional imaging methods, we can obtain the shear wave velocity distribution from Green's functions.

1.2   Green's Function

Green's Function (GF) [Green, 1854] between receivers can be estimated using seismic interferometry (SI). It is an impulse response of the Earth between any two points, which is constructed by cross-correlation of a pair of seismic time series recorded at two different sensors [Dziewonski and Anderson, 1981, Schuster and Snieder, 2009]. It is used to study the Earth's elastic properties and provides insightful views of Earth's subsurface structure. The cross-correlation turns noise into the signal as if one of the receivers acted as a virtual sesimic source because of the absence of a real source. Such a source response is equivalent to the GF convolved with a wavelet. Hence, SI is called the Green's function retrieval. If the noise sources are uniformly and spatially distributed, then the cross-correlation of noise records gives us the wholesome GF of the medium [Wapenaar and Fokkema, 2006].

1.3   Nature of Ambient Noise

There are many ambient noise sources which depend on the frequency on which those are observed. Figure 1 shows the power spectral density of seismic noise. This spectrum shows two main peaks: the first peak called as primary microseisms, appears between 10 to 20 sec period, which is generated when ocean gravity waves interact with the seafloor and reach near-surface [Hasselmann, 1963]. The second peak of seismic noise is observed between 1 to 10 sec, known as secondary microseism. The interaction of ocean gravity waves having the same wavelength as previous and travelling in reverse direction generates the secondary microseism [Longuet-Higgins, 1950, Stutzmann et al., 2001, 2012]. The interference between this forward and backward propagating waves create the pressure on the ocean floor at a frequency twice as high as the swell. This pressure is transmitted into the ground in the form of seismic waves. Local meteorological phenomena like wind, rain etc. and anthropogenic entities like cars, factories, cities generate high-frequency seismic noise. The seismic noise is actually composed of surface waves because the noise sources are excited on the surface of the Earth. Significant contribution in microseism band of noise generated at seafloor comes from the fundamental mode. This ambient noise is an economical energy source that is usually regarded as not so usable and removed from seismic data for analysis because of non-impulsive nature.

1.4   Ambient Noise Surface Wave Tomography

Ambient Noise Surface Wave Tomography (ANSWT) results from the computation of cross-correlation between seismic traces recorded on all available station pairs and then the measurement of dispersive nature of group or phase velocity associated with Rayleigh waves [Bensen et al., 2007]. Seismic travel time can be obtained using this dispersion curves and travel time inversion results in the shear wave velocity distribution in the crust and uppermost mantle [Shapiro et al., 2005, Sabra et al., 2005b]. The vertical component cross-correlation of seismic noise at periods ranging between 5 and 50 sec for several station pairs measures the dispersion curves of fundamental surface wave mode. This emerges the rapid development of ambient noise surface wave tomography [Moschetti et al., 2007].

The thumb rule for tomography is, performing the forward problem calculation and solving the inverse problem [Borah et al., 2014]. In ANSWT, an estimate of travel time using surface wave dispersion curve is considered as forward problem. The travel times are calculated using Fast Marching Method [Sethian, 1999], which is based on grid-based Eikonal solver. After this, the travel times are inverted based on subspace inversion gradient methods to obtain the
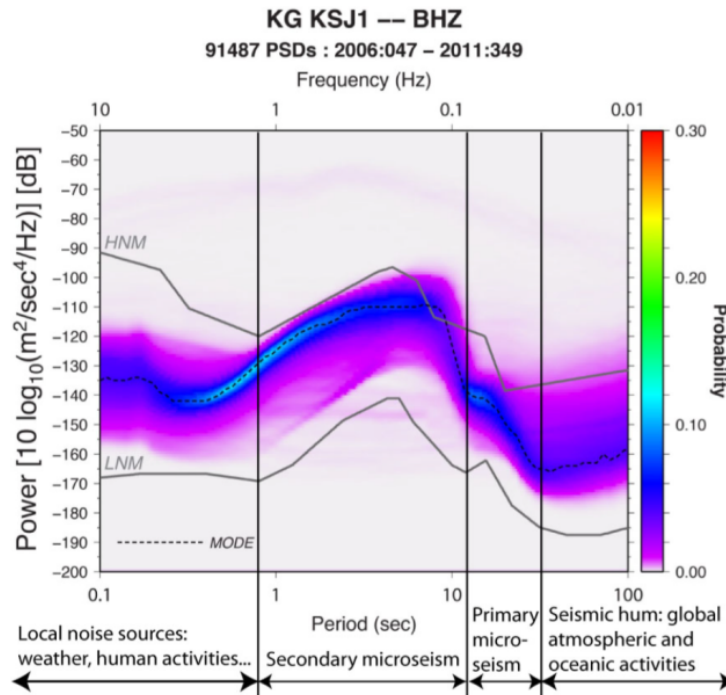
Figure 1 – Power spectral density of seismic noise recorded for 6 years on KSJ_1 station located in Antartica [Landès et al., 2010]

tomography image. This is done using Fast Marching Surface Tomography (FMST), Rawlinson and Sambridge [2004b].

1.5   Aim of the Thesis

The Mohorovičić discontinuity (Moho) has been mapped using joint inversion of receiver functions and Rayleigh wave group velocity beneath the East-West profile of South India at a depth of ~40 km which is thicker than that of the late-Archean crust [Saikia et al., 2016, 2017], but it didn't have the high resolution group velocity tomographic image at shallow depth (uppermost part of the crust). In our study, the main aim is to image the shallow Earth's crust (high frequency) beneath the East-West profile using cross-correlation of ambient noise and then by obtaining phase and group velocity maps at lower periods.

2 Geology of the study area

A craton is an old continental crust formed during Archean (2.5 Ga and older) and remained stable for over a billion years. The middle to late-Archean Dharwar craton is vital crustal block of the Indian subcontinent. Along the seismological profile (as shown in Figure 2), the most essential geological subunits are Archean Dharwar Craton (ADC) and the proterozoic Cuddapah Basin (CB). The Dharwar Craton (DC) consists of three different lithological units: (1) Tonalite-trondhjemite-granodiorite (TTG) Peninsular gneisses with composition of age between 3.36 and 2.7 Ga [Taylor et al., 1984]. (2) Volcano sedimentary greenstone belt having two different ages, 3.3-3.1 Ga and 3.2-2.7 Ga. (3) K-rich granitoids (N-S going Closepet Granite (CG)), having age 2.5-2.6 Ga. 2.7-2.5 Ga crustal block wraps the $\geq$ 3.4-3.0 Ga continental nucleus in the west part of DC [Beckinsale et al., 1980]. Gneiss, schist belts and diapiric trondhjemites are major rock types of DC. DC is divided into Eastern (EDC) and Western (WDC) domain by N-S orienting belt of Chitradurga Schist Belt (CSB) [Chadwick et al., 1992].

The neo-Archean WDC is surrounded to North by Deccan Volcanic Province (DVP) and Kaladgi Basin (KB), to the west by Konkan plane and Western Ghats (WG), to the east by Chitradurga Schist Belt (CSB) and to the south by Southern Granulite Terrain (SGT). The west end of WDC comprises of coastal plane and WG. The Western Ghats are elevated over 1000 m high and slope gently towards eastern side across the southern Indian peninsular tip. The Indian continent's rifting away from Madagascar around ~85 Ma formed the WG and the western coast of India [Storey et al., 1995]. The WDC is composed of Archean TTG gneisses, dated 3.3 to 3.4 Ga [Pichamuthu and Srinivasan, 1984]. The WDC contains Mesoarchean (3.4-2.7 Ga) volcano-sedimentary successions with the most important period of addition of juvenile crust during 3.35-3.0 Ga. The mantle is depleted beneath the WDC as early as 3.35 Ga, suggested by geochemical data [Boyet and Carlson, 2005]. It has been observed that the regional metamorphic grade has increased in the north from greenschist to amphibolite and granulite in the south of WDC [Stein et al., 2004].

On the other side, during 2.7-2.5 Ga, there was an extenssive juvenille magmatism in the EDC. This occured after global crustal growth peak around 2.7 Ga [Dey, 2013]. It is mainly composed of the Dharwar batholith (granite), greenstone belts and intrusive volcanic and middle Proterozoic to the recent sedimentary basins [Pichamuthu and Srinivasan, 1984]. The Proterozoic Cuddapah Basin (CB) and the Eastern Ghat (EG) wraps the eastern segment of EDC. The separation of Rodinia from assembly of Gondwana during 2.6 to 1.2 Ga formed the Eastern Ghats. The EG has most recently been affected by India–Antarctica rifting [Naqvi and Rogers, 1987]. The eastern part of CB is presented by thrust faults, and this basin is bounded by granitic gneisses, dykes and sills [Meert et al., 2010]. The dominant age of dyke swarms is ~ 2400 Ma and 1800-1100 Ma reported by Ravi Kumar and Singh [2010]. The CB has evolved from the first igneous activity in the form of the lava flow at about 1850 Ma. This has occured in the South-Western part of EDC [Chatterjee and Bhattacharji, 2001].

In 1970s, along the East-West profile of South India, crustal structure has been first time imaged using wide-angle reflection/refraction (Deep Seismic Sounding – DSS) study [Kaila et al., 1979]. Except toward the edges, the East-West profile lies on the flat terrian with an average elevation of ~600 m. Along the seismic profile, Kaila et al. [1979], Chowdhury and Hargraves [1981] inferred seven crustal–scale faults that offset the Moho by ~7 km. Here average Moho depth ranges from about ~36 km in EDC to ~41 km underneath the WDC. Using traveltime analysis, wide–angle seismic data was modelled to obtain Moho depth [Mall et al., 2012, Chandrakala et al., 2015]. There was an argument for the presence of high-velocity layer (HVL, Vp > 7.0 km/s) at the base of the crust in some part of the profile, like beneath the WDC, CB and the EG. The thickness and velocity of layered Earth beneath the profile is poorly constrained
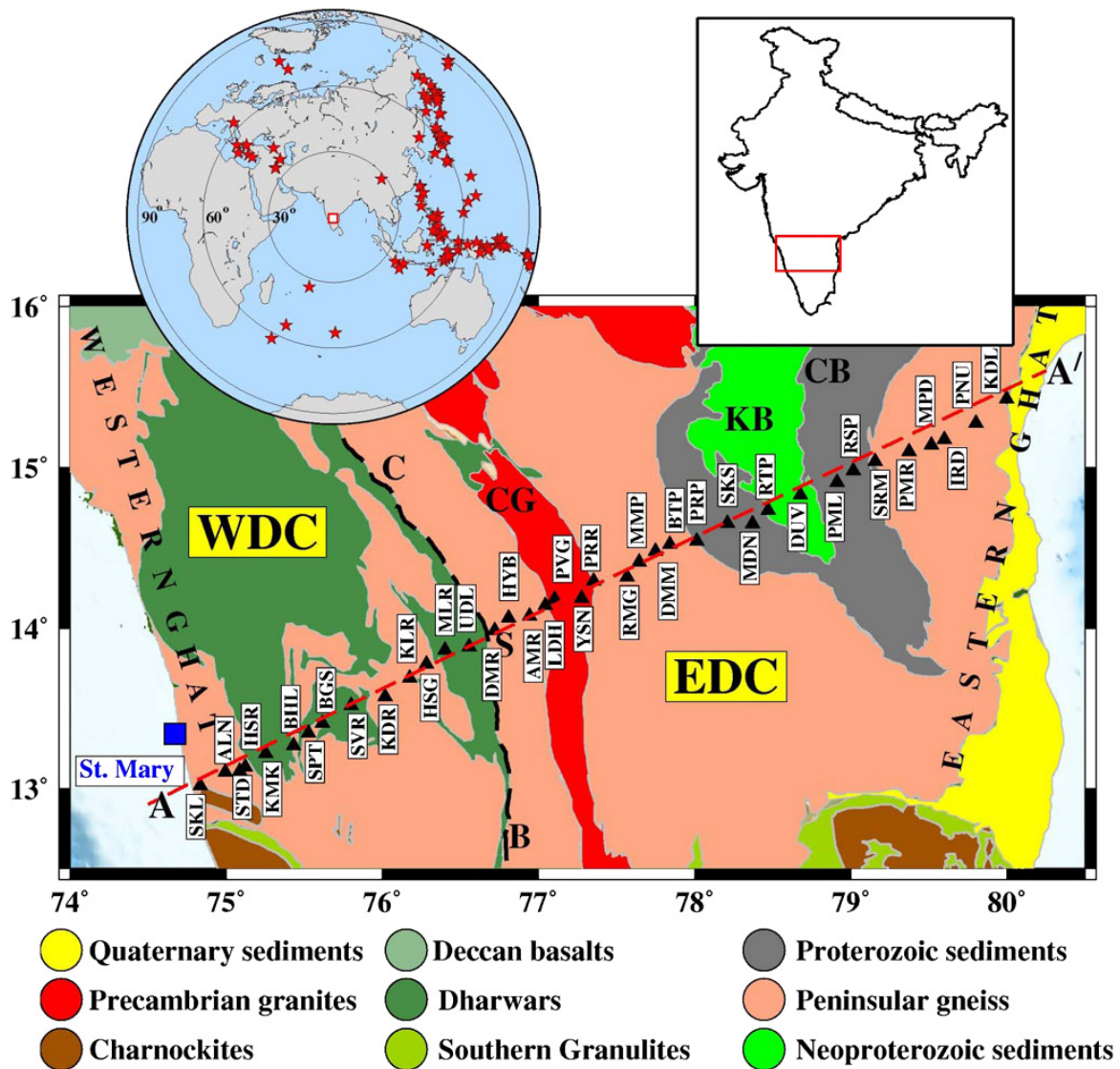
Figure 2 – Geological map showing major features along the seismic profile AA' are: Western Dharwar Craton (WDC), Eastern Dharwar Craton (EDC), Cuddapah Basin (CB), Chitradurga Schist Belt (CSB, marked by the dashed black line), Closepet Granite (CG). 38 seismic stations are shown by black triangles with three-letter code. The upper right inset is a map of India showing the study region (marked by the red square). This figure is modified from [Saikia et al., 2016]

due to some limitations in the quality of data and insufficient ray coverage. The Moho depth variation along the profile has been mapped using frequency analysis and common conversion point migration of receiver functions [Saikia et al., 2016].

3   Theory

3.1   Terminologies

3.1.1   Cross-Correlation

Cross-correlation calculates the similarity between two signals with respect to the time lag of one signal with respect to another. In mathematics, it is also called a sliding dot product [Proakis, 2001]. Here, term sliding defines the shift in the time. Higher the value of cross-correlation, higher is the similarity of two signals. The cross–correlation of a signal with itself is called as auto-correlation. In auto–correlation, there will always be a peak at a time lag of zero and it is called as the energy of signal as it will be square of the amplitude of signal [Gubbins, 2004].

Suppose we have two signals $x(t)$ and $y(t)$, then the cross–correlation $z(t)$ is given as:

$$z(t) = x(t) \otimes y(t) \equiv \int_{-\infty}^{\infty} x^*(\tau) y(\tau + t) d\tau \tag{1}$$

If we replace τ by $\tau - t$, then equation 1 becomes

$$z(t) = x(t) \otimes y(t) \equiv \int_{-\infty}^{\infty} x^*(\tau - t) y(\tau) d\tau \tag{2}$$

In the equations 1 and 2, t defines the time lag between two signals (this means the delay of x versus y). The $*$ denotes the complex conjugate of time series.
Convolution defines how the shape of one signal gets modified by other signal and it is given by:

$$x(t) * y(t) = \int_{-\infty}^{\infty} x(\tau) y(t - \tau) d\tau \tag{3}$$

If we compare equation 2 and 3, unlike the convolution, the integration variable, τ, has the same sign in the time arguments of $x(t)$ and $y(t)$ in cross-correlation. This means arguments will have a constant difference (in the case of correlation) instead of constant sum (convolution). The signal in cross-correlation will not be time flipped and will be time-flipped in convolution.

3.1.2   Green's Function

Green's Function (GF) is a solution to an inhomogeneous differential equation with a driving term given by delta function [Arfken and Weber, 1999]. It is an impulse response obtained using specified initial and boundary conditions. GF, $G(x, s)$, of a linear differential operator L acting on distributions over a subset of Euclidean space, at a point s, is a solution of

$$LG(x, s) = \delta(s - x) \tag{4}$$

where δ is the Dirac delta function [PA, 1941]. This property of a GF can be used to solve differential equations of the form [Arfken and Weber, 1999]:

$$Lu(x) = f(x) \tag{5}$$

3.2 Cross-Correlation Theorem

The retrieval of surface waves dispersion properties in subsoil using noise was first proposed by Aki and Richards [2002]. In the random wavefield, we acquire the GF of medium using cross-correlation of time series recorded between any two points. It includes reflection, scattering and propagation modes [Weaver and Lobkis, 2005]. In order to prove that the GF can be estimated from the stack of cross-correlations of noise records, different mathematical approaches were developed [Weaver and Lobkis, 2001, Snieder, 2004] and various assumptions were made about noise characteristic properties of the medium [Yao et al., 2009].

It is commonly believed that the diffuse wave fields reveal no information about the medium in which they propagate. But in ultrasonics, it was shown that the noise correlation function gives the waveform that would be obtained in a direct measurement [Weaver and Lobkis, 2001]. After this, [Campillo and Paul, 2003] applied this technique in seismology with real data and thus started a new branch of ambient noise tomography. For cross-correlation theorem, we follow the derivation proposed by [Gouedard et al., 2008].
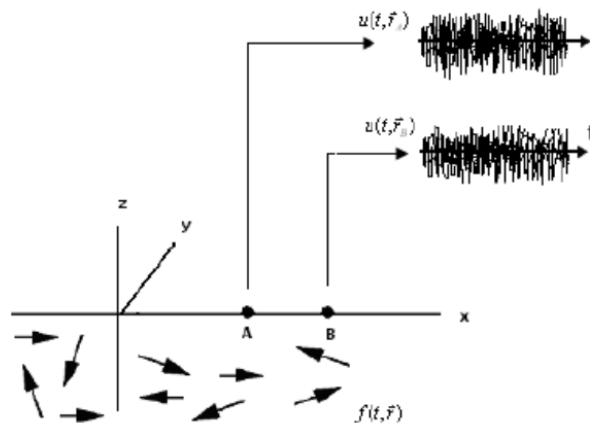
Figure 3 – Noise wavefields recorded at stations A and B are given by $u(t, \mathbf{r_A})$ and $u(t, \mathbf{r_B})$

Displacement fields $x(t, r_A)$ and $x(t, r_B)$ recorded at two receivers at locations A and B in a medium with a random noise field $f(t, r)$, (which is white noise distributed all over the medium) are shown in Figure 3. The time–domain cross-correlation between the two receiver locations can be defined as:

$$C(\tau, \mathbf{r_A}, \mathbf{r_B}) = \lim_{T \to \infty} \frac{1}{T} \int_0^T x(t, \mathbf{r_A}) x^*(t + \tau, \mathbf{r_B}) dt \qquad (6)$$

The $*$ denotes the complex conjugate. The displacement $x(t, \mathbf{r})$ is given using the Green's function G_a (a defines the attenuation for the convergence of integral) [Roux et al., 2005a].

$$x(t, \mathbf{r}) = \int_0^\infty dt' \int_X G_a(t', \mathbf{r}, \mathbf{r_s}) f(t - t', \mathbf{r_s}) d\mathbf{r_s} \qquad (7)$$

Here f defines the noise starting from $\mathbf{r_s}$ distributed in the medium X, acting at any time t. Here t' and $\mathbf{r_s}$ are integral variables over time and space respectively. Using equation 7, the definition of cross-correlation (equation 6) becomes,

$$C(\tau, \mathbf{r_A}, \mathbf{r_B}) = \lim_{T \to \infty} \frac{1}{T} \int_0^T dt \int_0^\infty ds \int_X d\mathbf{r_s} G_a(s, \mathbf{r_A}, \mathbf{r_s}) f(t - s, \mathbf{r_s})$$
$$* \int_0^\infty ds' \int_X d\mathbf{r_s}' G_a^*(s', \mathbf{r_B}, \mathbf{r_s})' f^*(t + \tau - s', \mathbf{r_s}') \tag{8}$$

If we consider the medium is damping, the large T limit in the correlation is replaced by an average ensemble, which gives the expectation value denoted by $\mathbf{E}$. As f is white noise, we obtain:

$$\lim_{T \to \infty} \frac{1}{T} \int_0^T f(t - s, \mathbf{r_s}) f(t + \tau - s', \mathbf{r_s}') dt = \mathbf{E}[f(t - s, \mathbf{r_s} f(t + \tau - s', \mathbf{r_s}')]$$
$$= \sigma^2 \delta(\tau + s - s') \delta(\mathbf{r_s} - \mathbf{r_s}') \tag{9}$$

where σ is a variance of the white noise. This will give us:

$$C(\tau, \mathbf{r_A}, \mathbf{r_B}) = \sigma^2 \int_0^\infty ds \int_X d\mathbf{r_s} G_a(s, \mathbf{r_A}, \mathbf{r_s}) G_a^*(s + \tau, \mathbf{r_B}, \mathbf{r_s}) \tag{10}$$

By using the expressions of GF in an attenuated medium, GF of positive and negative lags are obtained as [Snieder, 2004, Roux et al., 2005b]:

$$\frac{d}{d\tau} C(\tau, \mathbf{r_A}, \mathbf{r_B}) = -\frac{\sigma^2}{4a} (G_a(\tau, \mathbf{r_A}, \mathbf{r_B}) - G_a(-\tau, \mathbf{r_A}, \mathbf{r_B})) \tag{11}$$

The first one is called as causal GF and the second one is called anti-causal GF. When we have small enough damping coefficient and all noise sources behave like white noise in the medium, we obtain GF of the medium between two stations A and B by computing time-derivative of the cross-correlation between the wavefields recorded at those two stations. In the context of seismology, the GF of a medium between two points A and B represents the recorded signal at A if an impulsive source is applied at B. This illustration is shown in Figure 4 [Weaver and Lobkis, 2001].
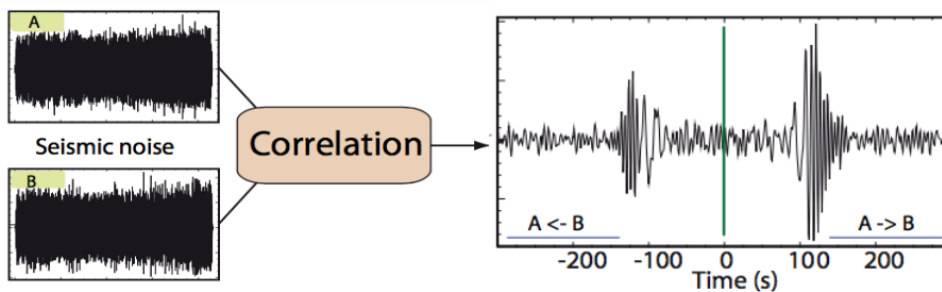
Figure 4 – Left: Seismic noise recorded at sensors A and B. Right: Cross-correlating both the signals results in causal and anti-causal Green's functions
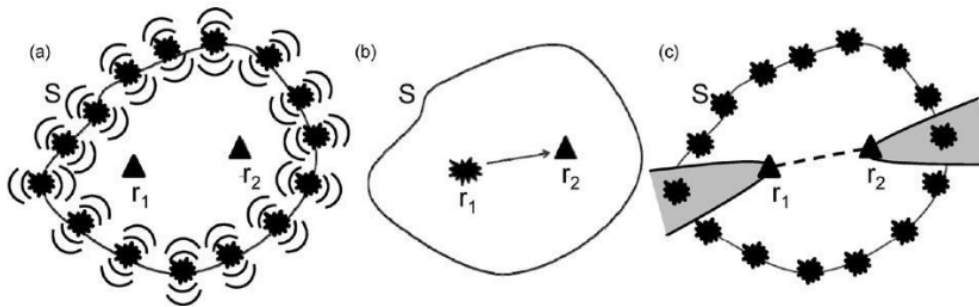
Figure 5 – (a): Two receivers (marked by black triangles and positioned at $\mathbf{r_1}$ and $\mathbf{r_2}$ are surrounded by boundary S of noise sources. (b): Receiver at $\mathbf{r_1}$ turned into the virtual source (real seismogram) by seismic interferometry. (c): Sources located within the grey regions contribute the most to Green's function

3.3   Formulation of Seismic Interferometry

The basics and fundamentals of seismic interferometry is to estimate the GF between any two seismic sensors by cross-correlating the ambient noise recorded on those sensors. In simple words, GF is considered as the recording of seismogram at one location because of the impulsive source of energy at the other location.

Now consider the following scenario. Suppose we have two receivers at positions $\mathbf{r_1}$ and $\mathbf{r_2}$ in the space which are surrounded by energy sources located in an arbitrary space with the boundary S, as shown in Figure 5. The wavefield starting from sources on boundary S propagates inside the medium and is recorded by both the receivers. One can compute the cross-correlation of signals recorded at both the stations. After adding together the cross-correlations for all the sources on boundary S the wavefield propagating towards the path of the receivers will add constructively (rise in the energy) and the rest will be destructively added (fall of the energy). This will result in the GF between two receivers as if one receiver acts like and source and other as receiver [Wapenaar, 2003, 2004]. If we consider the random noise, all the noise sources will shoot at the same time or overlapped shifted time, the energy from all sources will add together naturally [Wapenaar, 2004]. The seismic sources located randomly around the inter-receiver path gives us the interferometric GF between two receivers. Thus all the sources are not required to obtain the GF between two receivers [Snieder, 2004].

To elaborate more on seismic interferometry, we have used the demonstration of one-dimensional seismic interferometry given in [Wapenaar, 2004]. Figure 6 shows the plane wavefront, radiated by an impulsive unit source at $\mathbf{x} = \mathbf{x_s}$ and $t = 0$, propagating along the positive x-axis direction. Following assumptions are made: propagating velocity c is constant and no attenuation inside the medium. $\mathbf{x_A}$ and $\mathbf{x_B}$ are the positions of two receivers along the x-axis. The figure 6 shows the plane wave recorded first on the receiver at $\mathbf{x_A}$ which is given by Green's function $G(\mathbf{x_A}, \mathbf{x_s}, t)$. The definition of GF is given by impulse at $t_A = (\mathbf{x_A} - \mathbf{x_s})/c$ and hence it is given by Dirac delta function $G(\mathbf{x_A}, \mathbf{x_s}, t) = \delta(t - t_A)$, where t_A defines the arrival time of wave at $\mathbf{x_A}$. Similarly, the impulse response at $\mathbf{x_B}$ is given by $G(\mathbf{x_B}, \mathbf{x_s}, t) = \delta(t - t_B)$, where t_B defines the arrival time of wave at $\mathbf{x_B}$ and given by $t_B = (\mathbf{x_B} - \mathbf{x_s})/c$.

Looking at figure 6, the ray path from $\mathbf{x_s}$ to $\mathbf{x_A}$ associated with two GFs, $G(\mathbf{x_A}, \mathbf{x_s}, t)$ and $G(\mathbf{x_B}, \mathbf{x_s}, t)$ is common. Due to this, traveltime and wavefield from $\mathbf{x_s}$ to $\mathbf{x_A}$ will be shared and get cancelled after computing the cross-correlation, leaving only the traveltime between two receivers $\mathbf{x_A}$ and $\mathbf{x_B}$. This gives us the impulse response at t_B and t_A, shown in the figure. This impulse will be the response of source at $\mathbf{x_A}$, observed by the receiver at $\mathbf{x_B}$, which is
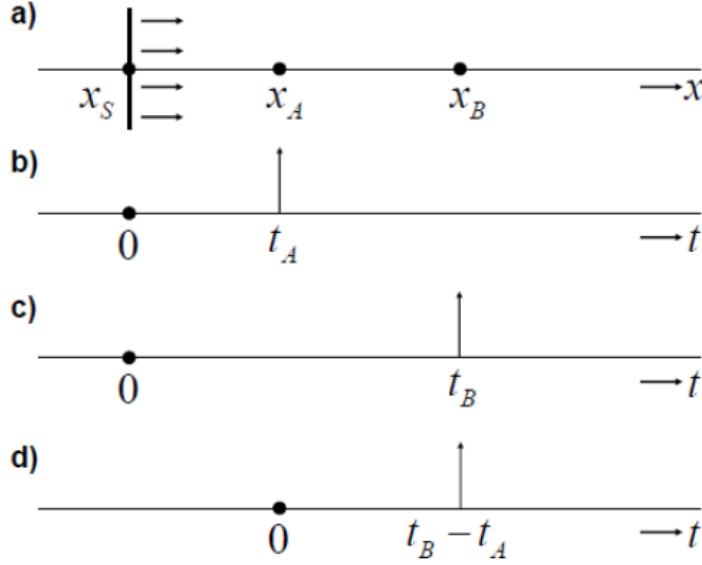
Figure 6 – Seismic interferometry in 1D: (a): Plane wavefront emitted by the source at $\mathbf{x_s}$ and two receivers are kept at positions $\mathbf{x_A}$ and $\mathbf{x_B}$. (b) and (c): t_A and t_B denote the recording time when the wave arrives at $\mathbf{x_A}$ and $\mathbf{x_B}$ respectively. (d): The cross-correlation delay is given by $t_B - t_A$

given in terms of GF $G(\mathbf{x_B}, \mathbf{x_A}, t)$ [Wapenaar, 2004].

Because both wave path and traveltime from $\mathbf{x_s}$ to $\mathbf{x_A}$ are common which get cancelled in cross-correlation, we don't need to know the propagation velocity c and the actual position $\mathbf{x_s}$ of source. The traveltime along the common path from $\mathbf{x_s}$ to $\mathbf{x_A}$ cancel each other cause it is not dependent on the propagation velocity and the length of the wave path. If the source impulse occurred at $t = t_s$ instead of at $t = 0$, the impulses observed at $\mathbf{x_A}$ and $\mathbf{x_B}$ would be shifted by the same amount t_s, which will be cancelled in cross-correlation which means absolute time t_s need not be known.

Now, let us define the cross-correlation of impulse responses at $\mathbf{x_A}$ and $\mathbf{x_B}$ as $G(\mathbf{x_B}, \mathbf{x_s}, t) * G(\mathbf{x_A}, \mathbf{x_s}, -t)$. Here the asterisk symbol denotes the temporal convolution of two signals with the time reverse of second GF. This converts convolution into cross-correlation which is given by:

$$G(\mathbf{x_B}, \mathbf{x_s}, t) * G(\mathbf{x_A}, \mathbf{x_s}, -t) = \int_{-\infty}^{\infty} G(\mathbf{x_B}, \mathbf{x_s}, t + t') * G(\mathbf{x_A}, \mathbf{x_s}, t') dt' \tag{12}$$

After using the definitions of delta function we get

$$G(\mathbf{x_B}, \mathbf{x_s}, t) * G(\mathbf{x_A}, \mathbf{x_s}, -t) = \int_{-\infty}^{\infty} \delta(t + t' - t_B)\delta(t' - t_A) dt'$$
$$= \delta(t - (t_A - t_B)) = \delta(t - (\mathbf{x_B} - \mathbf{x_A})/c) \tag{13}$$

which results in

$$G(\mathbf{x_B}, \mathbf{x_s}, t) * G(\mathbf{x_A}, \mathbf{x_s}, -t) = G(\mathbf{x_B}, \mathbf{x_A}, t) \tag{14}$$

This equation 14 signifies that the cross-correlation of signals at two receivers x_A and x_B gives the response at one of those receivers ($\mathbf{x_B}$) as if there was a source at ($\mathbf{x_A}$). Hence, SI called Green's function retrieval.

Suppose, the source waveform function is defined by source wavelet $s(t)$, then the displacement response at $\mathbf{x_A}$ and $\mathbf{x_B}$ can be written as

$$u(\mathbf{x_A}, \mathbf{x_s}, t) = G(\mathbf{x_A}, \mathbf{x_s}, t) * s(t) \tag{15}$$
$$u(\mathbf{x_B}, \mathbf{x_s}, t) = G(\mathbf{x_B}, \mathbf{x_s}, t) * s(t) \tag{16}$$

Let $S_s(t)$ be the autocorrelation of wavelet of the source function:

$$S_s(t) = s(t) * s(-t) \tag{17}$$

The cross-correlation between two displacements $u(\mathbf{x_A}, \mathbf{x_s}, t)$ and $u(\mathbf{x_B}, \mathbf{x_s}, t)$ is given by

$$u(\mathbf{x_B}, \mathbf{x_s}, t) * u(\mathbf{x_A}, \mathbf{x_s}, -t) = G(\mathbf{x_B}, \mathbf{x_s}, t) * s(t) * G(\mathbf{x_A}, \mathbf{x_s}, -t) * s(-t) \tag{18}$$

$$u(\mathbf{x_B}, \mathbf{x_s}, t) * u(\mathbf{x_A}, \mathbf{x_s}, -t) = G(\mathbf{x_B}, \mathbf{x_s}, t) * G(\mathbf{x_A}, \mathbf{x_s}, -t) * s(t) * s(-t) \tag{19}$$

Using equation 14 and 17, we obtain,

$$u(\mathbf{x_B}, \mathbf{x_s}, t) * u(\mathbf{x_A}, \mathbf{x_s}, -t) = G(\mathbf{x_B}, \mathbf{x_A}, t) * S_s(t) \tag{20}$$

3.3.1 Example Scenarios

Example 1   Consider the first example of noise correlations in a medium with random sources [Garnier and Papanicolaou, 2009]. Figure 7 shows the homogeneous medium with two sensors $\mathbf{x_1}$ and $\mathbf{x_2}$ and recorded seismic noise generated by sources all over the space. If the noise distribution is homogeneous around the sensors, then causal and anti-causal parts of correlation are identical. Another Figure 8 shows the noise sources are spatially localized and are stronger at the sensor $\mathbf{x_1}$. Here the correlation is not symmetric and causal GF is stronger. The situation will be reversed if the sources were near to $\mathbf{x_2}$. In cross-correlation, only the source aligned with the two stations contribute to the emergence of GF. The source distribution shown in Figure 7 is ideal situation; significant departures can occur and affect the quality of Green's function. In figure 8 he noise sources are not homogeneously distributed but have at least relatively uniform azimuth and correlation has amplitude asymmetry. The phase of the correlation remains unchanged on either side that allows evaluating the travel time of the waves and can be used in tomography [Garnier and Papanicolaou, 2009, Weaver et al., 2009, Froment et al., 2010].
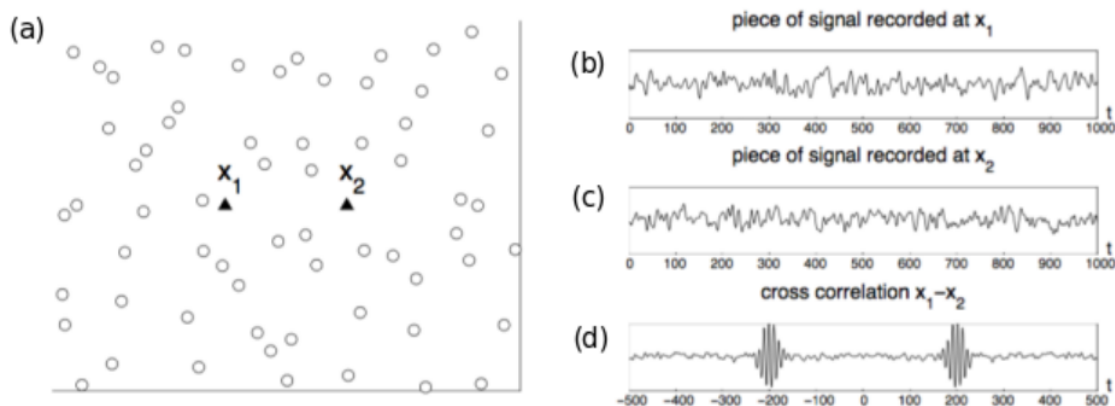
Figure 7 – (a): A medium with a homogeneous distribution of noise sources (circles) and $\mathbf{x_1}$ and $\mathbf{x_2}$ are receivers. (b) and (c): Seismic noise recorded at $\mathbf{x_1}$ and $\mathbf{x_2}$ respectively. (d): The causal and anti-causal part of Green's function
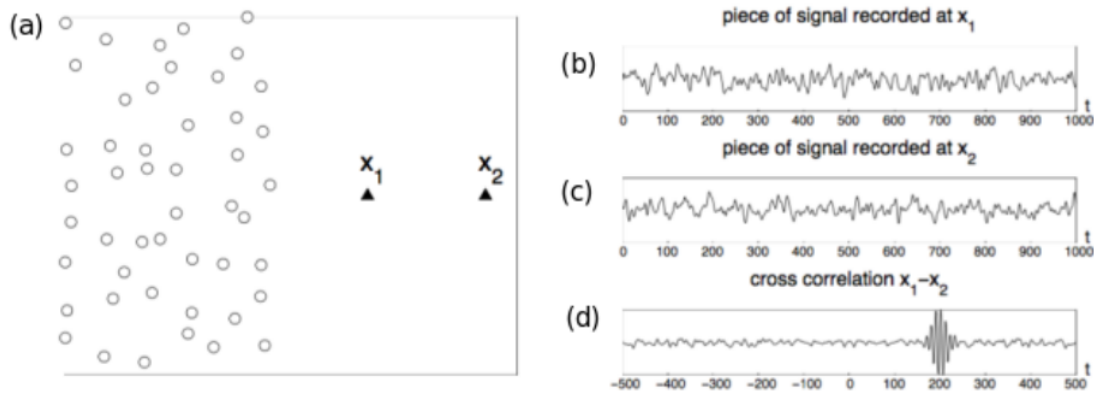
Figure 8 – (a): A medium with a inhomogeneous distribution of noise sources (circles) and $\mathbf{x_1}$ and $\mathbf{x_2}$ are receivers. (b) and (c): Seismic noise recorded at $\mathbf{x_1}$ and $\mathbf{x_2}$ respectively. (d): The causal and anti-causal part of Green's function

Example 2 In Figure 9, the wavefield emitted from a source at position $\mathbf{x_s}$ got recorded on receivers $\mathbf{x_A}$ and $\mathbf{x_B}$. These receivers are kept 1200 m apart from each other. The waveform shown in the figure is shifted by 0.6 sec and after computing the cross-correlation, we get the impulse response at 0.6 sec ahead of $t = 0$. This 0.6 sec delay defines the traveltime between positions $\mathbf{x_A}$ and $\mathbf{x_B}$. If we divide the distance between two receivers (1200 m) by traveltime obtained from Green's function (t = 0.6 sec), we obtain the propagation velocity of 2000 m/s. This velocity estimation suggest us the direct-wave interferometry can be used for tomographic inversion [Wapenaar, 2004, Snieder, 2004].
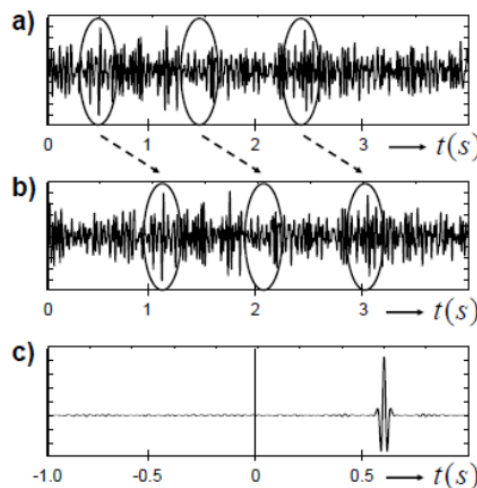
Figure 9 – (a) and (b): Seismic noise wavefield recorded first on the station at $\mathbf{x_A}$ and then on the station at $\mathbf{x_B}$. (c): Cross-correlation delay between signals at $\mathbf{x_A}$ and $\mathbf{x_B}$

3.4   An Overview of Surface Waves

There are two types of elastic waves [Aki and Richards, 2002]: First, P-waves, which involve the compression of elastic material in the direction of propagation of waves. Second, S waves, which include shear of elastic material perpendicular to the propagation direction. These two waves are collectively called as body waves. The interaction between this two waves while propagating through medium produces another type of elastic waves on the surface of elastic body.
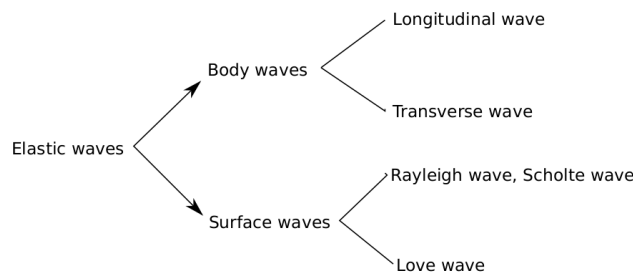
Figure 10 – Types of elastic waves

The surface waves mainly involve Rayleigh waves and Love waves. Here, Rayleigh waves have displacement perpendicular to propagation direction whereas Love waves have displacement along the direction of propagation. Surface waves have higher amplitude than that of the body waves because they travel through the surface while body waves travel through the interior of the earth. Figure 10 shows the principal types of elastic waves propagating in the earth.

3.4.1   Types of Surface Waves

1. **Rayleigh Waves:** Rayleigh waves are named after Lord Rayleigh [Strutt, 1885], who predicted the existence of this wave mathematically in 1885. Rayleigh waves travel up and down with an elliptical and retrograde particle motion confined to the vertical plane in the propagation direction near the surface of a homogeneous half-space [Stein and Wysession, 2009]. These are vertically polarized waves. These waves are generated by the superposition of P and SV waves aligned with the wave propagation direction. SV waves are S-waves (body waves) propagating in the vertical plane. Figure 11a shows the particle motion of Rayleigh waves.

2. **Love Waves:** Love waves were named after A.E.H. Love, a British mathematician, who mathematically solve the model for this wave in 1911 [Sokolnikoff et al., 1956]. Love waves have a particle motion, which is transverse to the propagation direction but with no vertical motion, therefore, it is a horizontally polarized wave with SH motion. Their side-to-side motion (like a snake wriggling) causes the ground twisting, and that is why Love waves cause much damage to structures during earthquakes. Figure 11b shows the particle motion of Love wave.

3. **Scholte Waves:** Scholte waves are the interface (for example water and solid) waves, the intensity of the wavefield mainly encountered at the interface and ceases exponentially above and below that [Scholte, 1947]. The Scholte waves have the same property as of Rayleigh waves, but the Scholte wave velocity is lower than the lowest velocity in the medium [Biot, 1952].

Surface waves travel through the surface of the earth and mostly confined in outer layers [Stein and Wysession, 2009]. These waves cause the destruction and damage associated with the earthquakes. In the case of far-field, surface waves have lower frequency content than the body waves and can be distinguished in seismograms. The surface waves are dispersive, which means their propagation velocity will depend on the frequency content in the wave. This is because a finite duration wave changes its shape during propagation in a dispersive medium due to its individual spectral components travel with distinct velocities. The distortion of waves sometimes causes some problems in the signal transmission and the precise measurement in the transmission of signals. However, this dispersive nature of surface waves is essential for tomographic imaging of the earth's crust.
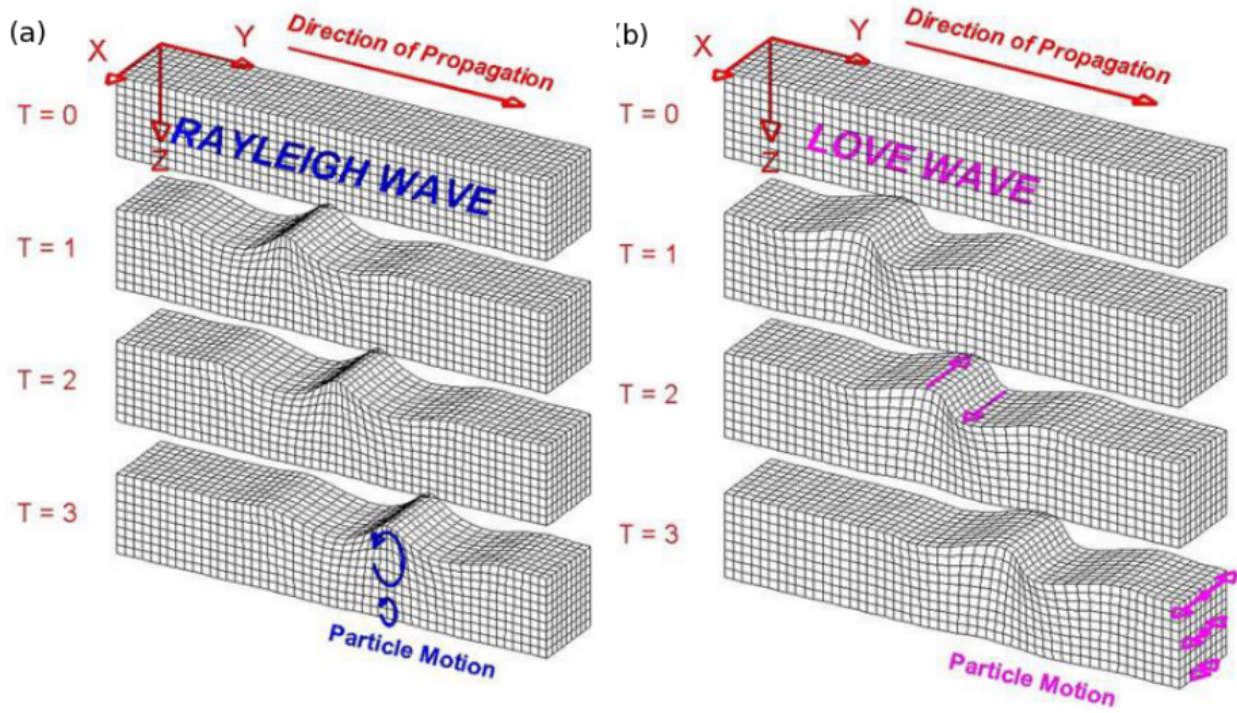
Figure 11 – The particle motion of (a) Rayleigh waves and (b) Love waves. Here T denotes different time values. The figure is adapted from http://www.geo.mtu.edu/UPSeis/waves.html

3.4.2 Wave Propagation

The equations governing the wave propagation in seismology are: First one is for compressional P-waves with scalar potential $\phi(\mathbf{x}, t)$:

$$\nabla^2 \phi(\mathbf{x}, t) = \frac{1}{\alpha^2} \frac{\partial^2 \phi(\mathbf{x}, t)}{\partial t^2} \tag{21}$$

Here α defines the compressional wave velocity which is given by:

$$\alpha = \sqrt{\frac{\lambda + 2\mu}{\rho}} \tag{22}$$

where λ and μ are Lammés Parameters and ρ is the density of a medium. Second one is for shearing S-waves with vector potential $\mathbf{\Gamma}(\mathbf{x}, t)$:

$$\nabla^2 \mathbf{\Gamma}(\mathbf{x}, t) = \frac{1}{\beta^2} \frac{\partial^2 \mathbf{\Gamma}(\mathbf{x}, t)}{\partial t^2} \tag{23}$$

Here β defines the shear wave velocity which is given by:

$$\beta = \sqrt{\frac{\mu}{\rho}} \tag{24}$$

To understand the propagation of both body waves through elastic earth medium, consider the plane wave propagating in the $\mathbf{z}$-direction (vertically down). The scalar potential for P wave satisfying equation 21 is given as:

$$\phi(z, t) = A e^{i(\omega t - kz)} \tag{25}$$
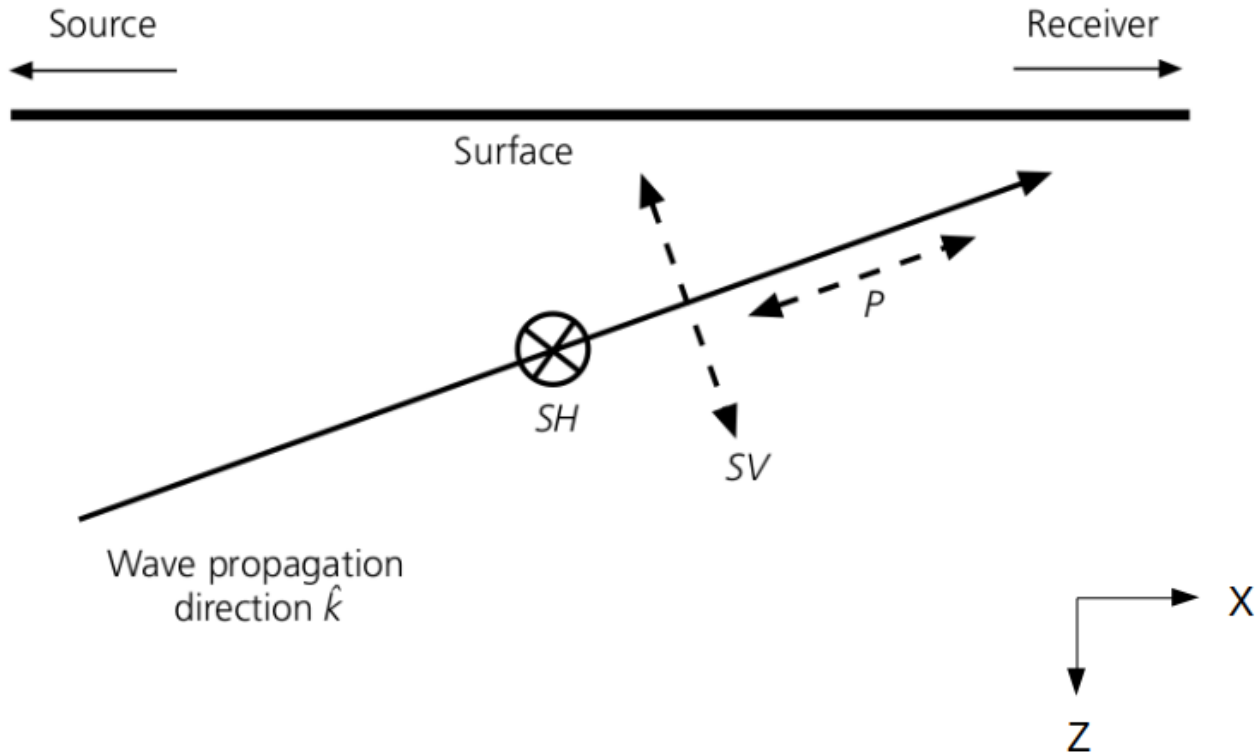
Figure 12 – P and S waves are propagating in the $x - z$ plane which contains the source and receiver. The P wave displacement is along the wave vector k. Perpendicular to wave vector, S wave is decomposed into SV and SH polarization. The horizontal polarization is SH and the vertical polarization is SV

where A is the amplitude, ω is frequency content of the wave and k is the wavenumber. The displacement corresponding to this scalar potential is given by its gradient

$$u(z,t) = \nabla\phi(z,t) = (0,0,-ik)Ae^{i(\omega t - kz)} \tag{26}$$

This displacement has a non-zero component only along the propagation direction **z**. The vector potential satisfying shear wave equation 23 is given by:

$$\mathbf{\Gamma}(z,t) = (A_x, A_y, A_z)e^{i(\omega t - kz)} \tag{27}$$

The resulting displacement field is given by curl of vector potential

$$u(z,t) = \nabla \times \mathbf{\Gamma}(z,t) = (ikA_y, -ikA_z, 0)e^{i(\omega t - kz)} \tag{28}$$

whose component along the propagation direction is zero. Thus the only displacement associated with propagating shear wave is perpendicular to the propagation direction. The plane waves travelling on a direct path between the source and the receiver thus propagate in the $x - z$ plane. There are two types of polarization for S waves: **SV waves** (vertically polarised waves), shear waves with displacement in the vertical $(x - z)$ plane and **SH waves** (horizontally polarised waves), shear waves with displacement in the horizontal y-direction. The polarization direction of both P and S waves is shown in Figure 12.

In the interior of the earth, P and SV waves are coupled to each other as they propagate in the same plane (X-Z) and when they occur on the earth's surface, this coupling produces

the Rayleigh waves. However, the SH wave is not coupled to any of the wave as it travels perpendicular to the X-Z plane and when it arrives at earth's surface, it becomes **Love Wave**. One can extract useful information about the crust and upper mantle using the dispersive nature of these waves. Rayleigh waves exist in half-space and do not show the dispersive nature if we consider the half space model. However, in case of a layered model of earth Rayleigh wave becomes dispersive in nature.

3.4.3   Rayleigh Waves in Half Space

Rayleigh waves are the result of a superposition of P and SV waves. In $x - z$ plane, consider the wave propagating in the **x**-direction. The potential associated with P wave motion is given by

$$\phi = Ae^{(-ikrz+ik(x-ct))} \tag{29}$$

Similarly the potential associated with S wave motion is

$$\psi = Be^{(-iksz+ik(x-ct))} \tag{30}$$

Here A and B are wave amplitudes, k is the wavenumber, c is the apparent velocity of the wave along x-axis, α is P wave velocity, β is S wave velocity and finally r and s defines the ratio of vertical to horizontal wavenumbers for P and S waves respectively and they are given by

$$r = \sqrt{\frac{c^2}{\alpha^2} - 1} \qquad\qquad s = \sqrt{\frac{c^2}{\beta^2} - 1} \tag{31}$$

For solving the wave equation (differential equation) using P and S wave potential, we need to consider the following boundary conditions:

1. Energy does not propagate away from the surface   For this is to happen, energy needs to be trapped near the surface. That means exponentials e^{-ikrz} and e^{-iksz} must have negative real exponents so that displacement will tend to zero as $z \to \infty$. As r and s given by equation 31, it requires $c < \beta < \alpha$, so that both the square roots in equation 31 become imaginary like

$$r = -i\sqrt{\frac{c^2}{\alpha^2} - 1} \qquad\qquad s = -i\sqrt{\frac{c^2}{\beta^2} - 1} \tag{32}$$

Here, apparent velocity c, should be less than that of the shear wave velocity

2. Free Surface Boundary Condition   This is equivalent to vanishing the traction vector at the free surface, i.e., at $z = 0$, the vertical stress components $\sigma_{xz}, \sigma_{yz}, \sigma_{zz}$ must be zero for all x and y. σ_{yz} will be automatically zero as there will not be any y component for both P and SV waves. We can describe the vertical stress components in terms of potentials by

$$\sigma_{xz} = 2\mu e_{xz} = \mu \left(\frac{\partial u_x}{\partial z} + \frac{\partial u_z}{\partial x} \right) = \mu \left(2\frac{\partial^2 \phi}{\partial x \partial z} + \frac{\partial^2 \psi}{\partial x^2} - \frac{\partial^2 \psi}{\partial z^2} \right) = 0 \tag{33}$$

$$\sigma_{zz} = \lambda\theta + 2\mu e_{zz} = \lambda \left(\frac{\partial^2 \phi}{\partial x^2} + \frac{\partial^2 \phi}{\partial z^2} \right) + 2\mu \left(\frac{\partial^2 \phi}{\partial z^2} + \frac{\partial^2 \psi}{\partial x \partial z} \right) = 0 \tag{34}$$

Here λ and μ are Lammés parameters, θ is dilatation and e is strain vector. By substituting the ϕ and ψ potentials into above equations of stress components, we obtain:

$$2rA - (1 - s^2)B = 0$$
$$[\alpha^2(r^2 + 1) - 2\beta^2]A - 2\beta^2 sB = 0 \tag{35}$$

Here we obtain two equations and two unknowns, so other than the trivial solution, we obtain unique solution for this equations by equating the determinant to be zero:

$$\begin{vmatrix} 2r & -(1 - s^2) \\ \alpha^2(r^2 + 1) - 2\beta^2 & 2\beta^2 s \end{vmatrix} = 0$$

Solving this determinant gives us

$$[\alpha^2(r^2 + 1) - 2\beta^2](1 - s^2) - 4rs\beta^2 = 0 \tag{36}$$

If we substitute the values of r and s from equation 32 into equation 36, we obtain

$$\left(2 - \frac{c^2}{\beta^2}\right)^2 = 4\sqrt{1 - \frac{c^2}{\alpha^2}}\sqrt{1 - \frac{c^2}{\beta^2}} \tag{37}$$

This is called *Rayleigh's Equation*. Here the apparent velocity is constant, i.e., it is not a function of either wavenumber $c(k)$ or frequency $c(\omega)$. The Rayleigh wave velocity is related to body waves velocity using Poisson's ratio (ratio of α/β). As body wave velocities are constant, independent of depth, the Rayleigh wave velocity in homogeneous half-space is independent of frequency.

3.4.4 Rayleigh waves in an elastic layer over half space
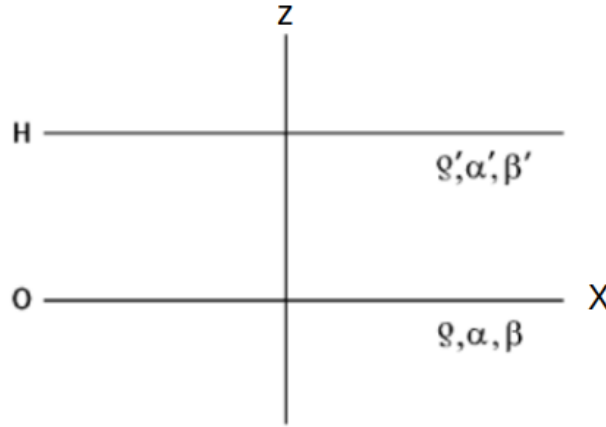
A layer of thickness $z = H$, with density ρ', P wave velocity α' and S wave velocity β', over the elastic half space $z = 0$ with density ρ, P wave velocity α and S wave velocity β

Consider a layer of thickness $z = H$, with density ρ', P wave velocity α' and S wave velocity β', over the elastic half-space with density ρ, P wave velocity α and S wave velocity β. One thing to note here is that the wave will propagate in both positive and negative z-direction, but will only travel in positive the z-direction in half-space (as shown in Figure 3.4.4). After defining this geometry of layers, we can define the potentials in the following way: First, the potentials in half-space are

$$\phi = Ae^{(-ikrz - ik(x - ct))} \tag{38}$$
$$\psi = Be^{(-iksz - ik(x - ct))} \tag{39}$$

The potentials in layer of thickness $z = H$ are

$$\phi' = A'e^{(ikr'z-ik(x-ct))} + B'e^{(-ikr'z-ik(x-ct))} \tag{40}$$

$$\psi' = C'e^{(iks'z-ik(x-ct))} + D'e^{(-iks'z-ik(x-ct))} \tag{41}$$

where the definitions of r, s, r', s' are given by

$$r = -i\sqrt{\frac{c^2}{\alpha^2} - 1} \qquad s = -i\sqrt{\frac{c^2}{\beta^2} - 1} \qquad r' = -i\sqrt{\frac{c^2}{\alpha'^2} - 1} \qquad s' = -i\sqrt{\frac{c^2}{\beta'^2} - 1} \tag{42}$$

Since the amplitude of the wave decreases with the depth in the half-space, the r and s should be positive and imaginary. This will happen only if $c < \beta < \alpha$. To obtain the solutions for above potentials, we need to find exact expressions for the amplitudes A', B', C', D', A and B and to obtain this, following boundary conditions needs to satisfy

- At $z = H$, free boundary condition, all the stress components are zero

- At $z = 0$, continuity condition, all stress and displacement components are continuous

After applying these boundary conditions, we obtain the solutions for wave amplitudes, i.e., amplitudes in layer and half-space by equating the determinant of coefficients of amplitude to zero. This gives us the velocity of Rayleigh waves c as a function of wavenumber, $c(k)$. By this means Rayleigh waves become dispersive in the layer above the half space. The graphical solution for Rayleigh waves is shown in the figure 13. Here, the graph of velocity w.r.t. wavenumber is plotted. The dispersive nature of Rayleigh waves can be described using normal modes [Stein and Wysession, 2009] and these modes are marked by M_{11}, M_{12}, M_{21}, as shown in Figure 13. Here M_{11} is called as fundamental mode. These modes are of two types: *Symmetric modes*, in which vertical displacement at the contact between two surfaces have the opposite sign and *Asymmetric modes*, in which vertical displacement have the same sign.
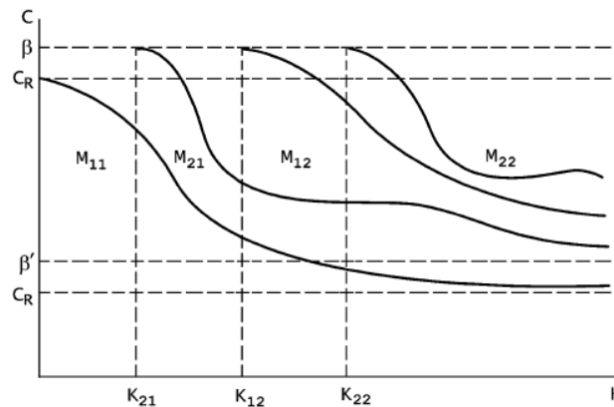
Figure 13 – Dispersion curve of normal modes associated with Rayleigh waves. M_{11} is a fundamental mode and rest (M_{12} and M_{21}) are higher modes (overtones). k_{11} and k_{12} and k_{21} are wavenumbers of normal modes. β' and β are S wave velocities in a layer of thickness $z = H$ and half-space respectively.

3.4.5 Surface wave dispersion

The sum of two harmonic waves with slightly distinct angular frequencies and wavenumbers is given by

$$u(x,t) = A\big[cos(\omega_1 t - k_1 x) + cos(\omega_2 t - k_2 x)\big] \tag{43}$$

The angular frequencies (ω_1 and ω_2) and wavenumbers (k_1 and k_2) can be written in terms of deviation from their respective average values:

$$\begin{aligned} \omega_1 = \omega + \delta\omega \qquad & \omega_2 = \omega - \delta\omega \qquad & \omega \gg \delta\omega \\ k_1 = k + \delta k \qquad & k_2 = k - \delta k \qquad & k \gg \delta k \end{aligned} \tag{44}$$

After putting this back to equation 43, we obtain

$$\begin{aligned} u(x,t) &= A\big[cos((\omega + \delta\omega)t - (k + \delta k)x) + cos((\omega - \delta\omega)t - (k - \delta k)x)\big] \\ &= 2A\big[cos(wt - kx)cos(\delta\omega t - \delta k x)\big] \end{aligned} \tag{45}$$

Thus the sum of two harmonic waves becomes the product of two cosine functions and the resultant waves are also propagating harmonic waves. As $\delta\omega$ is smaller than ω, second cosine term varies more slowly in time than that of the first one. Similarly, δk is smaller than k, the same cosine term varies more slowly in space and time than that of the first one. So this slower propagating wave will act as the envelope with frequency $\delta\omega$ and wavenumber δk over the faster propagating wave with frequency ω and wavenumber k. The envelope is superimposed over the faster propagating wave (carrier wave). The velocity with which this envelope travels is called *group velocity* which is given by $U = \delta\omega/\delta k$. The velocity with which carrier wave travels is called *phase velocity* which is given by $c = \omega/k$

3.4.6 Group Velocity Dispersion

The energy in the wave propagates as the envelope of wave packet at a velocity which is called group velocity. The packet of energy that propagates as a surface wave contains a spectrum of periods due to its dispersive nature. The period of the wave packet is measured from the time between successive peaks or troughs. The wave with the longest period travels faster and appears first on seismogram because of less attenuation through the medium. The straight forward way to calculate the group velocity is to divide the interstation distance by the travel time of the wave packet.

Example Suppose the distance between two stations is 1000 km, then the wave group with period 25 sec and travel time of 295 sec will have group velocity of $\frac{1000\ km}{295\ sec} = 3.38\ km/s$. The next arriving wave group with period 20 sec and travel time of 310 sec will have group velocity of $\frac{1000\ km}{310\ sec} = 3.22\ km/s$. This tells us that Rayleigh wave with different frequency or period travels with different velocity.

4   Fast Marching Surface Tomography

4.1   Background Information

After obtaining the dispersive nature of group/phase velocity dispersion curves from GF, we can calculate the travel time of Rayleigh waves. Inverting the travel times lead to determine the variations in group velocity at a particular frequency in the region of interest. By calculating the travel times for several frequencies, we can construct a 2D velocity model.

Tomography is a way to understand the internal (unknown) property of medium from line integral of the already known property of the medium. **Ex:** Suppose, we know the travel time of propagating seismic waves and we represent it using data, $\mathbf{d}$, then we can estimate the seismic wave velocity in the medium (which is represented by model parameters, $\mathbf{m}$) using the line integral of travel time in the medium over the path length. The linear relation between model parameters, $\mathbf{m}$ and data, $\mathbf{d}$ is given by:

$$\mathbf{d} = G\mathbf{m} \tag{46}$$

The relation between observed data, $\mathbf{d}_{obs}$ and the initial set of model parameters, $\mathbf{m}_o$ is also given by equation 46. Our main aim is to estimate the model parameters, $\mathbf{m}_{est}$ by minimizing the difference between $\mathbf{d}_{obs}$ and model data, $\mathbf{d}_{est}$. Here $\mathbf{d}_{est}$ is obtained using intial set of model parameters, $\mathbf{m}_o$. This is considered as an inverse problem where we update $\mathbf{m}_o$ subject to any regularization constraints. The protocol of several steps to produce a tomographic image from seismic data is [Rawlinson et al., 2003, Rawlinson and Sambridge, 2004a, Menke, 2018, Parker and Parker, 1994, Tarantola, 1987]:

1. **Model Parameterization:** The physical or seismic properties of the medium are defined by a set of model parameters and we need to specify them as a first step of tomography.

2. **Forward Calculation:** This defines the procedure for calculation of model data (synthetic data) given the set of values of model parameters.

3. **Inversion:** Regularization of model parameter values under the line of perfect matching of model/synthetic data with the observed data along with the specified constraints.

Let us understand all the above steps with the help of the following example: In tomographic imaging, consider traveltime as model data and velocity variations as model parameters. For a continuous velocity medium $v(x)$, the traveltime of a ray is:

$$t = \int_{L(v)} \frac{1}{v(x)} dl \tag{47}$$

where ray path is given by $L(v)$ and velocity field by $v(x)$. This equation is non-linear cause traveltime is inversely proportional to velocity.

This non-linear inverse problem can be converted to the linear inverse problem under the assumption that the path between source and receiver is unperturbed in great extent by adjusting the model parameter values in the inversion. For this, consider the perturbation in velocity as:

$$v(x) = v_0(x) + \delta v(x) \tag{48}$$

The path along which this integration is computed is given by:

$$L(v) = L_0 + \delta L \tag{49}$$

Similarly, the traveltime perturbation is given by:

$$t = t_0 + \delta t \tag{50}$$

Then equation 47 for determining travel time becomes:

$$t = \int_{L_0 + \delta L} \frac{1}{v_0 + \delta v} dl \tag{51}$$

By expanding the integrand using Geometric series and ignoring the higher-order terms (cause perturbation is low), we obtain:

$$\delta t = - \int_{L_0} \frac{\delta v}{v_0^2} dl + O(\delta v^2) \tag{52}$$

If we define slowness as the inverse of the velocity field, $s(x) = 1/v(x)$, the perturbation in traveltime is given by

$$\delta t = - \int_{L_0} \delta s \, dl + O(\delta s^2) \tag{53}$$

where δs is perturbation in slowness. Hence the traveltime perturbation δt is linearly dependent on the slowness perturbation δs. This also demonstrates the linearisation of non-linear inverse problem.

4.2   Description of steps for Tomography

4.2.1   Model Parameterization

The traveltime of a ray from source to receiver is governed by the velocity profile of the medium. This results in representing the subsurface structure of the earth by variations in wave velocity or slowness. These variations notify the velocity parameterization. The possible ways to define the velocity parameterization are:

1. **Constant velocity blocks**, which defines the ray paths within each and every block. These blocks are not the first choice for representation of smooth variations in subsurface structure due to discontinuities in velocity field velocity that resides between adjacent blocks.

2. **Use interpolation function**, which helps to define velocity values at the vertices of a rectangular grid. If we demand to have continuous first and second derivatives in the velocity field, then its better to use higher order interpolation functions. They are used in ray tracing method [Thomson and Gubbins, 1982].

Some other uncommon velocity parameterization are:

- Define the velocity variations using a set of interfaces whose geometry is varied to satisfy the data

- A specific combination of velocity and interfaces parameters.

We can define the above listed velocity parameters with the help of *a priori* information in either of the forms given below:

- Presence of natural boundaries like faults or interfaces

- Adequate data coverage to resolve the trade-off between interface and velocity

- Pre-defined protocol of inversion routine

4.2.2   Fast Marching Method: Forward Problem for Traveltime

In tomography, forward problem is defined by the traveltime calculation between known end-points through given medium. There are many ways of determining source-receiver traveltimes like ray tracing (bending and shooting of ray), wavefront tracking schemes (finite difference solutions of Eikonal equation). There are certain drawbacks in this method of ray tracing like robustness, speed and uniqueness of the derived ray paths. To overcome these drawbacks, Rawlinson et al. [2003], Rawlinson and Sambridge [2004a] used Fast Marching Method (FMM) and then the inversion is carried out [Sethian, 1996]. This method is a variant of wavefront tracking. This method was initially developed by [Sethian and Popovici, 1999] for tracking advancing interfaces.

For tracking the evolution of monotonically advancing interfaces via the finite difference solution of Eikonal equation, we can use a grid-based numerical scheme, FMM [Sethian, 1999, Rawlinson et al., 2003]. The Eikonal equation [Tarantola, 1987] states that the magnitude of the travel time gradient at any point along a wavefront is the inverse of the velocity at that point which can be given as:

$$|\nabla_x T| = \frac{1}{v(x)} = s(x) \tag{54}$$

where ∇_x is a gradient operator, T is traveltime and $s(x)$ is slowness. There is no direct solution for this Eikonal equation cause $\nabla_x T$ is not defined when we consider the gradient discontinuities. So another way to solve the Eikonal equation is to use a weak form of solution which results in continuous traveltime vector $T(x)$ and may not have continuous $\nabla_x T$. One way to obtain the solution is to introduce the viscous term in the Eikonal equation

$$|\nabla_x T| = s(x) + \epsilon \nabla_x^2 T \tag{55}$$

where ϵ is a viscous limit and put constraints on the smoothness of the solution. We obtain the weak solution corresponding to the first-arriving wavefront in the limit of smooth solution. This approach of a weak form of solution is used by [Sethian and Popovici, 1999] to solve the Eikonal equation on a 3D grid. This means FMM uses the first-order upwind difference scheme:

$$\sqrt{max\left[D_{ijk}^{-x}T, -D_{ijk}^{+x}T, 0\right]^2 + max\left[D_{ijk}^{-y}T, -D_{ijk}^{+y}T, 0\right]^2 + max\left[D_{ijk}^{-z}T, -D_{ijk}^{+z}T, 0\right]^2} = s_{ijk} \tag{56}$$

where s_{ijk} is the slowness at the grid point $(i,\ j,\ k)$. Other terms are given by:

$$D^{+x}T = \frac{T(x+\delta x) - T(x)}{\delta x} \qquad\qquad D^{-x}T = \frac{T(x) - T(x-\delta x)}{\delta x} \tag{57}$$

where T is traveltime and δx is grid spacing. As shown in Figure 14 upwind scheme indicates that if wave progress from left to right. We should use finite difference scheme that reaches upwind to the left to get information to construct the solution downwind to the right. This scheme tells us how to calculate new traveltimes if we know the traveltime on the adjacent grid points. One important thing is to note that the order in which grid points are updated should be in the direction of flow (either upwind or downwind). In this method, the grid points on which first true traveltime arrives are *alive* grid points. All neighbouring points of one of the *alive* point are *close* points on which traveltimes are correctly assigned. The points on which we compute the traveltime for the first time and which are away from *close* points are *far* points. In the flow of calculations, *far* points become *close* points. The calculation scheme will continue until all of the *far* points become *alive* points; hence, the propagation of wavefront is traced in the whole medium.
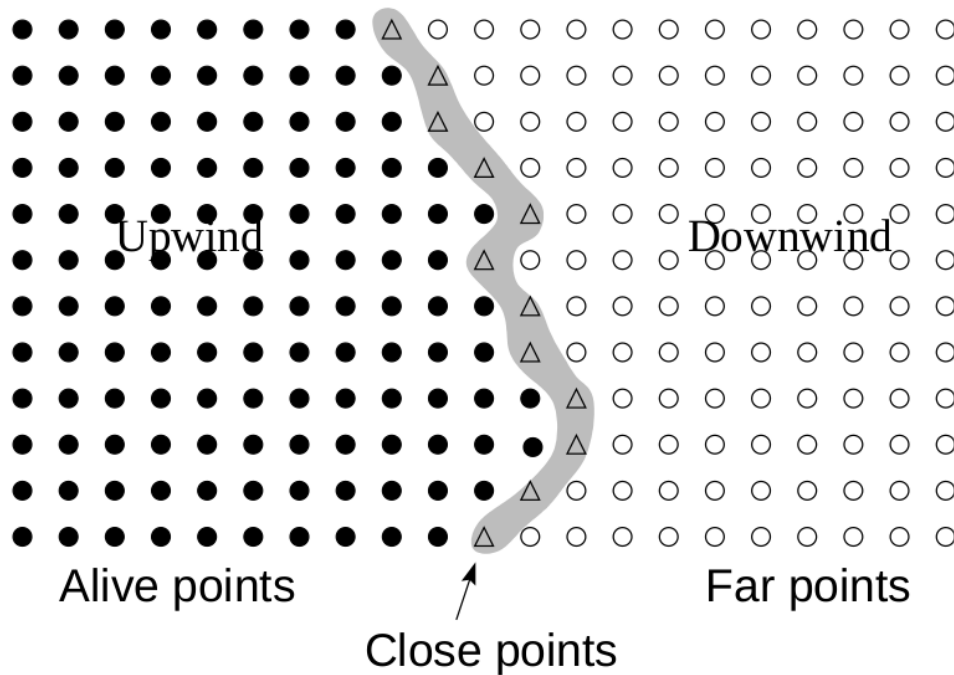
Figure 14 – Illustrating the method of narrow band. The traveltimes for *Alive* points are accurately calculated. *Close* points form a band about the *alive* points and they are assigned by trial values. None values are calculated for *Far* points. *Alive* points lie upwind of the narrow band whereas far points lie downwind. The figure is adapted from [Rawlinson et al., 2003]
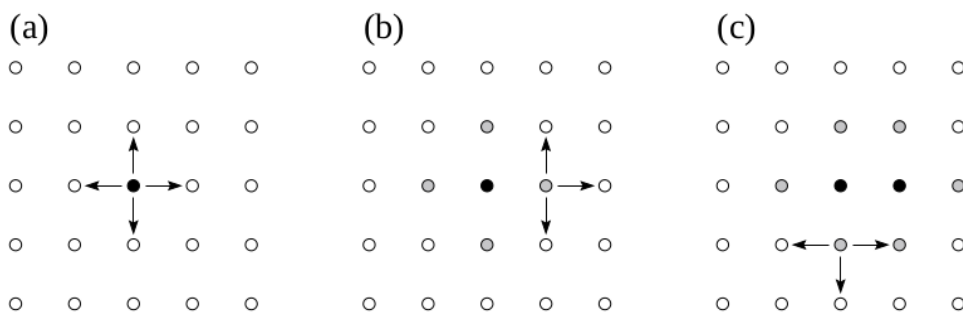
Figure 15 – Illustration of the FMM in 2-D. (a): The traveltimes at four neighbouring points of source point (black dot) are estimated using Eq. 34. (b): The smallest of these four values (grey dots) should be correct, so all *close* neighbours to this point that are not *alive* (white dots) have their values computed, and added to the narrow band defined by the grey dots. (c) The smallest of these six *close* points again must be correct, and all neighbouring points have their values computed (or recomputed). The figure is adapted from [Rawlinson et al., 2003]

Figure 15 illustrates the evolution of narrow-band method to solve the Eikonal equation in the medium with the help of waveform given on the source point. Choosing the *close* points with the least traveltime means the causality of wave propagation is satisfied. This also guarantees *alive* points are evaluated with the causal information. The *close* point with minimum travel time is all the time upwind to the adjacent *close* points. Once the travel time between on all the grid points is calculated, we invert it using subspace inversion.

4.2.3 Traveltime Inversion

Inversion is the technique where the misfit between model parameters **m** and observed data **d_obs** needs to be minimized. The relation between **m** and **d** is given by

$$\mathbf{d} = G\mathbf{m} \tag{58}$$

where G is called a data kernel. The inversion can be performed in various ways: back-projection method, gradient methods, global optimization. For traveltime inversion, we follow here the inversion based on the gradient method. In this case, the underlying medium is divided into 3D blocks where slowness can be defined. Suppose, the traveltime integral is discretized for a single ray in j^{th} block,

$$\delta t = - \int_{L_o} \delta s \; dl + O(\delta s^2) \tag{59}$$

The discretization of above continuous integral gives us

$$\delta t = \sum_j l_j \Delta s_j \tag{60}$$

where Δs_j is slowness in block j and l_j is the path length in the corresponding block. This equation can be written as $\mathbf{d} = G\mathbf{m}$, where **d** defines the perturbation in traveltime, **m** defines the model parameter matrix in terms of velocity perturbation and data kernel is defined by the path length l. The solution of $\mathbf{d} = G\mathbf{m}$ using generalized inverse method provides an estimate of the model parameter, $\mathbf{m}_{est}$ as

$$\mathbf{m}_{est} = \left[G^T G\right]^{-1} G^T \mathbf{d} \tag{61}$$

Then the misfit becomes $\mathbf{d}_{obs} - G\mathbf{m}_{est}$. Then we update **m** iteratively again by minimizing the new misfit until sufficient convergence is achieved. In traveltime tomography, the inverse problem is commonly underdetermined as the number of model parameters to be estimated is less than that of total number of observed data points. So to solve such an underdetermined problem, we need to define the objective function $S(\mathbf{m})$. Along with minimizing the misfit between observed data and estimated model parameters, introduce *a priori* information about the model parameters into the objective function as regularization term:

$$S(\mathbf{m}) = (\mathbf{d} - G\mathbf{m})^T (\mathbf{d} - G\mathbf{m}) + \epsilon (\mathbf{m} - \mathbf{m}_o)^T (\mathbf{m} - \mathbf{m}_o) \tag{62}$$

where ϵ is the damping parameter to control the underdetermined part of the solution and $\mathbf{m}_o$ is the *a priori* information about the model parameters to be estimated. The first term on the RHS of the above equation is misfit term, which implies minimizing the error between estimated and observed data. The second term is regularization term (norm of the model parameter) which helps to minimize non-uniqueness of the solution. The solution is obtained by minimizing the objective function. This involves minimizing misfit and regularization term simultaneously. The trade-off between both the terms is controlled by ϵ. When ϵ is large, the weight of norm increases compared with the misfit term, that is why we try to minimize the norm of the model parameters to more extent. When ϵ is less, weight of the misfit term increases compared with the norm term and we try to minimize misfit term to more extent. This method is called trade-off minimization [Menke, 2018].

5   Methodology

In this study, we have used a total of 38 seismic stations which were operated by the *Council of Scientific and Industrial Research - National Geophysical Research Institute* (CSIR-NGRI) along ∼660 km East-West profile. As shown in the Figure 2, this East-West profile mainly consists (from west to east) of Western Dharawar Craton, Eastern Dharawar Craton and Cuddapah Basin [Saikia et al., 2017, 2016]. We have used ambient seismic noise recorded on a total of 38 broadband seismic stations along the East-West profile (station list is described in Appendix A). Ambient noise data is a continuous recording of Earth's surface vibration for a year long period. We have considered only the vertical (Z) component data recorded on a seismic station. This noise data is cross-correlated and Green's functions have been extracted. These GFs are used to compute the dispersion curves. In this project work, we have used basic Linux© Shell scripting to edit, store and organize the data. For analysing seismic data, we have used Seismic Analysis Code (SAC) [Goldstein and Snoke, 2005]. SAC is the best tool for organizing, editing, processing seismic data. Generic Mapping Tool (GMT) [Wessel et al., 2013] is used to create geographical figures and plots. Various MATLAB© and Shell scripts are used for processing the seismic data.

For ambient noise data processing, we have used the procedure described by Bensen et al. [2007], shown in Figure 16.

This involves the sequence of the following steps:

1. Initial data preparation

2. Cross-correlation and temporal stacking

3. Computing travel times and phase/group velocity dispersion curves

4. Error analysis and quality control

After performing all the above steps, we follow the following steps to generate the tomographic image of the region of interest

1. Preparing group/phase velocity maps

2. Computing shear velocity maps

Now we will discuss all these steps in detail:

5.1   Initial data preparation

The initial step of data analysis is to prepare the waveform data for every individual station. This helps to generate the broad-band ambient noise by removing the earthquake signals and instrumental irregularities. It is more important when we have a period longer than the microseism band (∼5 to ∼17 sec). This step composed of few processing steps like removal of instrument response, mean and trend from the signal. This is followed by bandpass filtering, time-domain amplitude normalization and then spectral whitening of the seismic signal. This is applied on a single day seismic data.

Phase 1:

Raw data → Remove instrument response, remove mean, remove trend, band-pass filter, and cut to length of 1-day

Apply time domain normalization → Apply spectral whitening

Phase 2:

Compute cross-correlation → Stack day-correlations to desired number of days

Phase 3:

Measure group and/or phase velocity

Phase 4:

Error analysis → Selection of acceptable measurements
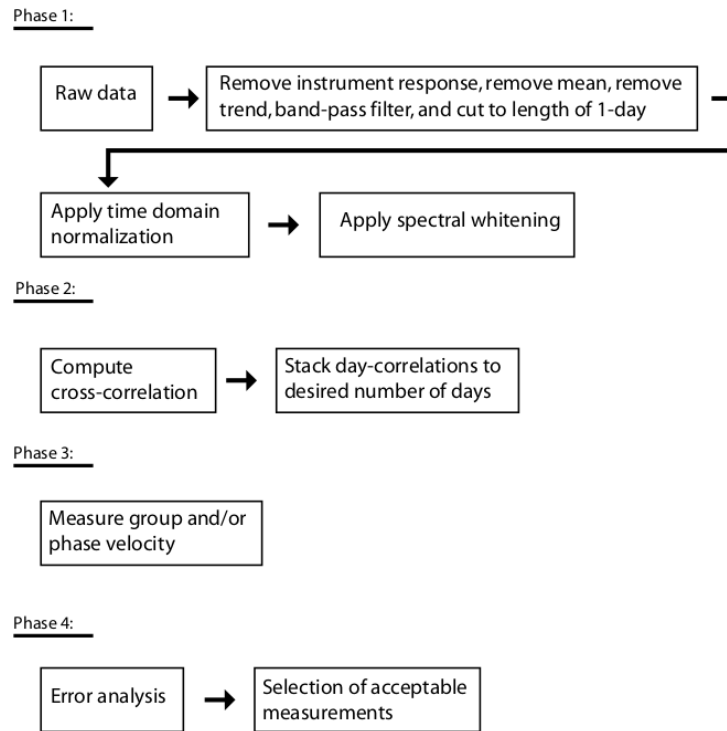
Figure 16 – Schematic illustration of the data processing scheme. The steps involved in preparing single-station data prior to cross-correlation are mentioned in Phase 1. Phase 2 shows us the procedure of cross-correlation and stacking. Phase 3 involves dispersion curve measurement and Phase 4 is the error analysis and data selection process. The figure is adapted from [Bensen et al., 2007]

5.1.1 Temporal Normalization

This is also called time-domain normalization. It reduces the effect of earthquakes, instrumental irregularities and non-stationary noise sources on cross-correlation. It uses the technique called *one-bit normalization*, which keeps only the sign of raw signal. This means replace all the positive amplitudes of signal by +1 and all the negative amplitudes by -1. This will helps to enhance the signal to noise ratio (SNR) [Larose et al., 2004, Yao et al., 2009]. This also helps to remove the narrow data glitches completely.

5.1.2 Spectral Normalization

Spectral normalization is also called whitening. It flattens down the amplitude spectrum by removing the seismic hum, primary and secondary microseism. It helps to stretch the band of the ambient noise signal in cross-correlation and combats the degradation caused by consistance monochromatic sources.

In our case, we had raw seismic data in *.ref* format. We converted it to *.sac* format using **ref2sac** code. The *.ref* data was continuous recording and while converting it to *.sac* format, we created a one-day (24 hour) long individual segments for each station. We have then removed the instrument response using the poles and zeros from the one-day long *.sac* data from all respective stations (This is exaplained in Appendix B). We applied tapering to remove the glitches at both the start and end of each of the one-day data. We have removed the mean from each data to get rid of the linear trend and to make the data centered to its zero amplitude. Then we applied the bandpass filter, temporal and spectral whitening to flatten down the microseism and seismic hum, which is present in the data.

5.2   Cross-Correlation

Here, we perform the cross-correlation between day long ambient noise data from all possible pairs of stations. Suppose we have n number of stations then it gives us a total of $n(n-1)/2$ station pairs. It is usually common to obtain millions of cross-correlations when we have ambient noise recorded on several seismic stations. This will produce a new time series in terms of GFs. The cross-correlations are two-sided time functions with both positive and negative correlation lags (shift from zero in opposite directions). The positive part of the cross-correlated signal is called *causal* signal and the negative part is called *anti-causal* signal. These represent the waveform propagating in opposite directions between signals. There are two methods of computing cross-correlations: Geometric cross-correlation and Phase cross-correlation [Schimmel, 1999].

5.2.1   Geometric Cross-Correlation (CCGN)

The Geometric Cross-correlation or CCGN is used because it is independent of amplitude changes in time series. The CCGN output ranges between +1 and -1, where +1 signifies the perfect matching of two time series with coherency (same polarity) and -1 signifies the matching of time series with the same coherency but with opposite polarity.

Suppose we have two time series, $s_1(t)$ and $s_2(t)$, the CCGN as a function of time t is given by:

$$C_{CCGN}(t) = \frac{\sum\limits_{\tau+\tau_0}^{\tau_0+T} s_1(t+\tau)s_2(\tau)}{\sqrt{\sum\limits_{\tau+\tau_0}^{\tau_0+T} s_1(t+\tau)^2 \sum\limits_{\tau+\tau_0}^{\tau_0+T} s_2(\tau)^2}} \tag{63}$$

where τ is summation index and τ_0 is the starting time of both the series $s_1(t)$ and $s_2(t)$. The summation of time series is performed over a time window of length T. Here the denominator is the geometric mean of energy of two time series.

5.2.2   Phase Cross-Correlation (PCC)

It is based on a complex trace (analytical signal) analysis. Suppose we have analytical signal $S(t)$. If we represent its real part by $s(t)$ and imaginary part by Hilbert Transform [Arfken and Weber, 1999] of $s(t)$ as $H\big[s(t)\big]$, then

$$S(t) = s(t) + iH\big[s(t)\big] = A(t)e^{i\phi(t)} \tag{64}$$

where $A(t)$ is time dependent amplitude which is also called envelope and $\phi(t)$ is instantaneous phase [Bracewell and Bracewell, 1986].

Suppose we have two signals $s_1(t)$ and $s_2(t)$, we then measure the phase stack coherence to determine the similarity at every sample

$$c(t) = \frac{1}{2N} \sum\limits_{\tau=\tau_0}^{\tau_0+T} |e^{i\phi(t+\tau)} + e^{i\psi(\tau)}| \tag{65}$$

where $e^{i\phi(t)}$ and $e^{i\psi(t)}$ are amplitude normalized analytic signals of $s_1(t)$ and $s_2(t)$. At time t the phase stack is calculated at each time sample τ for the time length of T. All N samples are added together and $1/2N$ is normalization factor. When two signals are perfectly coherent,

then $c(t)$ becomes 1 and when they are coherent with opposite polarity, then $c(t)$ becomes 0. This makes the amplitude 0, which should be 1 when signals are perfectly anti-correlated. We expand equation 65 to include anti-correlation part

$$C_{PCC}(t) = \frac{1}{2N} \sum_{\tau=\tau_0}^{\tau_0+T} \left\{ |e^{i\phi(t+\tau)} + e^{i\psi(\tau)}| - |e^{i\phi(t+\tau)} - e^{i\psi(\tau)}| \right\} \tag{66}$$

Using this equation, cross-correlated amplitude ranges between +1 (perfectly correlated) and -1 (perfectly anti-correlated).

5.2.3   Comparision between CCGN and PCC

Though CCGN and PCC are independent of amplitude content of signals, they differ from each other. PCC has high oscillation sensitivity whereas CCGN includes fast decay of oscillation at the end of narrow band wavelet. The SNR of the output of different cross-correlations depends on waveform complexity. The PCC is highly sensitive to waveform complexity and hence gives us a higher signal to noise ratio (SNR) than that of CCGN. The root mean square (RMS) ratios of CCGN to PCC are more than 1, which again interpreted as stronger sensitivity of waveform similarity in PCC measure. The CCGN gives higher cross-correlation by aligning the waveforms by their absolute maximum or minimum but not at the zero time lag. However, in PCC, we obtain higher cross-correlation when waveforms are aligned at zero time lag. Low amplitude noise within the correlation window will have its most definite impact when PCC is used and is equally sensitive to all perturbations in the wavelet. PCC permits discrimination between closely similar waveforms. This will have more advantage of travel time picking.

5.2.4   Stacking

The technique of combining a collection of cross-correlation traces into a single trace is called stacking [Bensen et al., 2007, Liu et al., 2009]. It is used to attenuate random noise and amplify the coherent signal. The stacking is a linear superposition method. We compute the cross-correlation of daily time series and then they are stacked further for whole available data. Stacking is the average trace of all available cross-correlate traces computed between a pair of stations over the prescribed time period. Suppose we have N number of cross-correlated traces $c(t)$, then linear stacking $c_s(t)$ is given by

$$c_s(t) = \frac{1}{N} \sum_{i=1}^{N} c_i(t) \tag{67}$$

where i is linear summation index.
In our study, we have used the stacking method called time-frequency phase-weighted stack (tf-PWS). We can improve the GF convergence when we have poor performance of traditional linear averaging methods using phase-coherence adapted by tf-PWS [Ventosa et al., 2017]. The phase-weighted stack (PWS) is an arithmatic product of linear stack and the phase stack [Schimmel and Paulssen, 1997]. The tf-PWS uses time-frequency expansion using S-transform [Stockwell et al., 1996] as it gives precise phase information.

5.3   Dispersion Curve Measurement

We obtain the Green's functions after computing daily cross-correlations and then stacking. The group and phase velocities are measured as a function of the period using Green's functions.

This can be done using Frequency Time Analysis (FTAN) [Dziewonski, 1971, Yanovskaya et al., 2012].

Suppose we have time series $s(t)$, its Fourier transform is

$$S(\omega) = \int_{-\infty}^{\infty} s(t)e^{(i\omega)t}dt \tag{68}$$

We obtain the dispersion measurements using the analytic signal which is given in the frequency domain by,

$$S_a(\omega) = S(\omega)(1 + sgn(\omega)) \tag{69}$$

The inverse Fourier transform of the above equation is:

$$S_a(t) = |A(t)|e^{i\phi(t)} \tag{70}$$

To construct frequency time function, we consider $S(w)$ subjected to narrow Gaussian bandpass filters with centre frequency ω_0

$$S_a(\omega, \omega_0) = S(\omega)(1 + sgn(\omega))G(\omega - \omega_0) \tag{71}$$

where Gaussian function $G(\omega - \omega_0)$ is given by

$$G(\omega - \omega_0) = e^{-\alpha\left(\frac{\omega - \omega_0}{\omega_0}\right)^2} \tag{72}$$

Here α defines frequency-time domain resolution, which is a function of the distance from source to receiver [Levshin et al., 1992]. We perform the inverse Fourier transform and it results in 2D smooth envelope function, $|A(t, \omega_0|$ and phase function $\phi(t, \omega_0)$. We obtain group velocity using $|A(t, \omega_0|$ and phase velocity using $\phi(t, \omega_0)$. The procedure for group and phase velocity dispersion measurements is different and we will see them individually.

5.3.1   Group Velocity Dispersion

It comprises a total of 8 steps which are described below:

1. FTAN graph is obtained by performing the log of the square of the envelope of the analytic signal, $log |A(t, \omega_0)|^2$. In this step, the group velocity is given by time t of the envelope function $A(t, \omega_0)$ and the period is given by center frequency ω_0.

2. Then track the dispersion ridge as a function of the period to get a raw group speed curve [Shapiro and Ritzwoller, 2002].

3. A phase-matched filter is defined in the chosen period band and applied to the waveform to obtain undispersed signal.

4. Identify the contaminated noise and remove from the undispersed signal. Here, noise comprises of earthquake signals, multi-path signals, coda waves, seismic waves.

5. Compute the FTAN image of the cleaned waveform by performing $log |A(t, \omega_0)|^2$ of the cleaned waveform. Here broader Gaussian filters (broader than which was applied to raw waveform) is applied to new waveform during phase-matched filtering.

6. Finally, track the dispersion ridge as a function of the period on the FTAN image to obtain final and filtered group velocity curve.

5.3.2   Phase Velocity Dispersion

Phase velocity measurements require the additional information along with the envelope function on which group velocity is measured. At instantaneous frequency ω

$$\phi(t,\omega) = k\Delta - \omega t - \phi_s - \phi_a \tag{73}$$

where traveltime is given by t, interstation distance by Δ, wavenumber by k, source phase by ϕ_s and phase ambiguity term by ϕ_a. When we observed phase at the observed group arrival time $t_u = \Delta/U$, and if $k = \omega s_c$, we write the expression for phase slowness as:

$$s_c = s_u + (\omega\Delta)^{-1}(\phi(t_u) + \phi_s + \phi_a) \tag{74}$$

Using phase slowness, we obtain phase velocity. For cross-correlations of ambient noise source phase is zero: $\phi_s = 0$. The 2π ambiguity part inherent to any phase spectrum gives us the phase ambiguity term as $\phi_a = 2\pi N$, the value of N gives the closest relation between prediction and observation. These terms give us additional information w.r.t. group velocity so that we obtain phase velocity dispersion. In ambient noise cross-correlations velocity waveforms are back-shifted by $-\pi/4$, i.e., $\phi_a = 2\pi N - \pi/4$. Then phase slowness becomes

$$s_c = s_u(\omega\Delta)^{-1}(\phi(t_u) + 2\pi N - \pi/4) \tag{75}$$

5.4   Traveltime Inversion

After obtaining the phase and group velocity maps, we invert fundamental mode Rayleigh wave group and phase velocity using Fast Marching Method (FMM). It uses an Eikonal solver to compute traveltimes and then subspace scheme to solve the inverse problem [Young et al., 2011, Rawlinson and Sambridge, 2004b]. Three important factors are considered for traveltime inversion and plotting velocity fields:

1. Damping factor: To prevent the final solution output from staying too far from the initial model

2. Smoothing factor: To constrain the smoothness of the solution output

3. Dicing factor: To refer to the subsampling of continuous velocity field using cubic B-spline velocity patches. This will be used to interpolate the velocity grid.

This both are *ad hoc* variables, but they are used to obtain a smooth output that is not greatly perturbed from the initial model and to satisfy the data. The steps to follow for tomographic inversion are given below

- To compute traveltime by FMM, a grid-based Eikonal solver

- To construct initial model for inversion

- To obtain the measure of model roughness and smoothness

- To invert the dispersion data linearly (least square inversion)

- To plot either group or phase velocity maps using color contour maps

6   Results and Discussion

6.1   Ambient Noise

Ambient noise was recorded along the East-West profile of South India using a total of 38 seismic stations. The data is stored in *.sac* format at 50 samples per second (Sampling frequency: 50 Hz) between a period of 2nd April 2012 and 24th October 2013 (total 18 months). The data is available on 3 components, namely North-South, East-West and Vertical components. Here, we have used vertical component for cross-correlations. In Figure 17, we have shown an example of 24-hour long ambient noise recorded on three seismic stations, namely DMR, KLR and PMR.
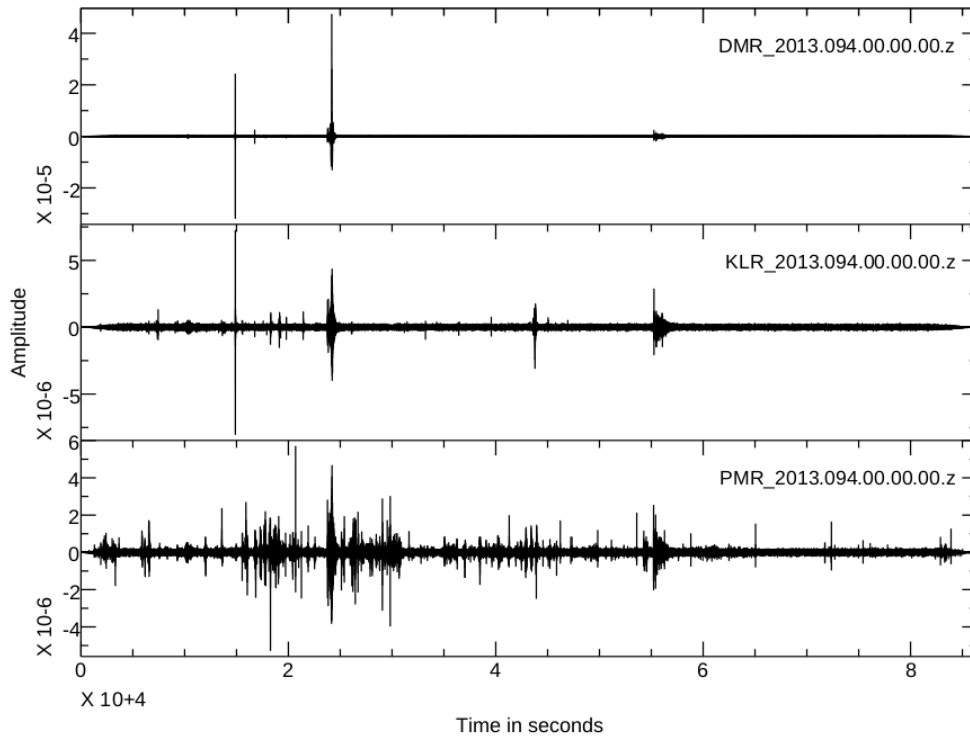
Figure 17 – Example of ambient noise recorded on 3 stations (DMR, KLR and PMR) on Z component

6.2   Cross Correlation and Stacking

We computed the cross-correlations of ambient noise as described in Bensen et al. [2007]. The instrumental response is corrected by removing poles and zeros from station data. Then the mean and trend were removed from data. The data has been downsampled from 50 Hz to 5 Hz. Then one-bit normalization is applied to data. In total, we had ambient noise recorded on 38 seismic stations and hence, we have 38*(38-1)/2 = 703 correlation pairs. We have computed two types of cross-correlations namely Geometric Cross-Correlation (CCGN) and Phase Cross-Correlation (PCC). Then we have stacked the cross-correlation output between all available pairs of seismic stations using tf-PWS method to improve the SNR of GF. We have performed two types of stacking using tf-PWS. In the first case, we obtained one-sided Green's functions (causal part), which signifies the seismic signal travelling from one station to another. In the second case, we obtained both the causal and anti-causal part of Green's function (symmetric GF), signifying that the seismic signal traveling between two stations to-and-fro. Thus we have obtained the following configurations of stacked Green's functions:

1. tf-PWS-CCGN (Geometrically cross-correlated with only causal part)

Figure 18 – Cross-correlation gather (CCGN) for the station ALN. Location of the station is shown in Figure 2. All cross-correlations are centered around zero time lag. The Green's functions are arranged according to an increasing distance between ALN and other stations

2. tf-PWS-CCGN-sym (Geometrically cross-correlated with causal and anti-causal part)

3. tf-PWS-PCC (Phase cross-correlated with only causal part)

4. tf-PWS-PCC-sym (Phase cross-correlated with both causal and anti-causal part)

Among these combinations, we have selected the Green's functions having a higher value of SNR. Example, suppose we have all 4 configurations of Green's functions between two stations, say ALN and AMR. If tf-PWS-CCGN-sym has higher value of SNR among all of them, then for further analysis, we have considered tf-CCGN-sym Green's function. Based on this criterion, out of 703 station pairs, we have chosen 700 for computing group and phase velocity dispersion. We have excluded the following station pairs: BHL-YSN, KMK-PVG, KLR-RSP. In Figure 18 and 19, we had shown the Green's functions obtained using CCGN and PCC technique between ambient noise recorded on ALN and rest all 37 stations, respectively. The Green's functions are arranged (top to bottom of Figure 18 and 19) according to the geographical distance between ALN station and other stations. If we compare both Figures 18 and 19, we observed here that the cross-correlations obtained using PCC are less noisy than that of obtained using CCGN. This here we preferred stacked Green's functions obtained using PCC over CCGN.

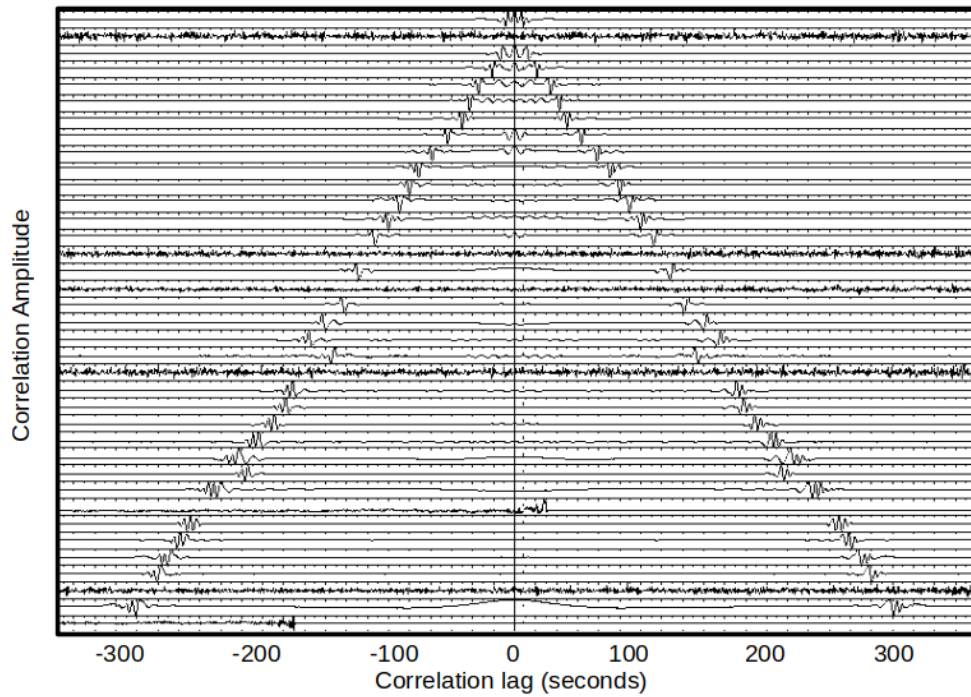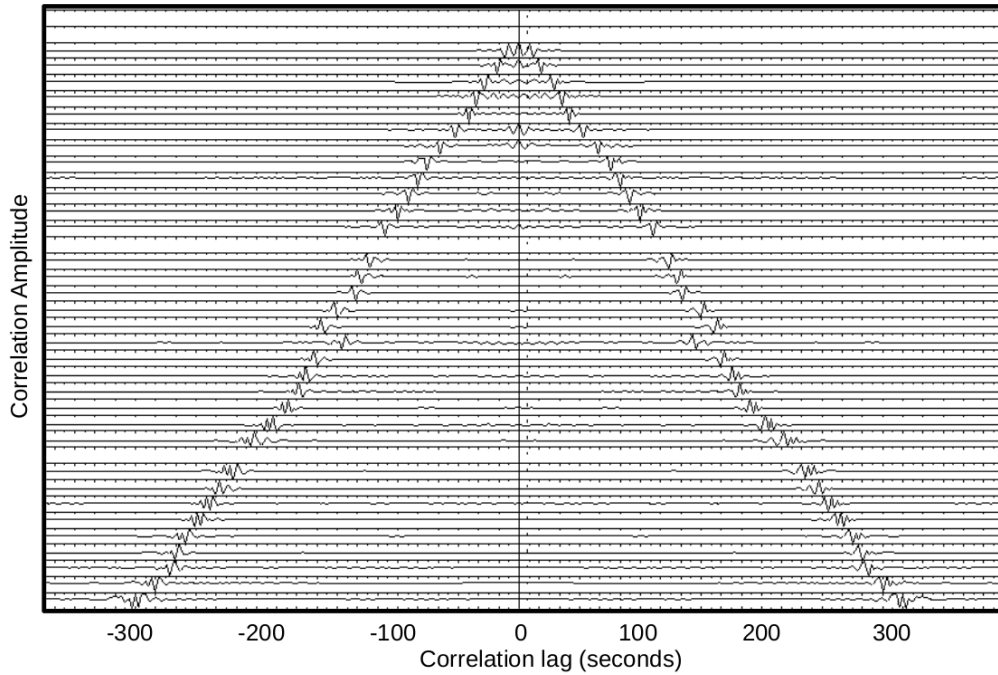Figure 19 – Cross-correlation gather (PCC) for the station ALN. Location of station is shown in Figure 2. All cross-correlations are centered around zero time lag. The Green's functions are arranged according to increasing distance between ALN and other stations

6.3   Dispersion of Group and Phase Velocity

The fundamental mode of both phase and group velocity dispersion curves is computed from stacked GF as described in sections 5.3.1 and 5.3.2. We have computed group and phase velocities by converting GFs into a frequency-time diagram of signal power as a function of frequency and group period. The period is extracted from the stacked Green's functions after applying Fourier transform on it. The central frequency in each Fourier transform is considered for the period. For the available stacked Green's functions, we have obtained a period from 3 sec to 18 sec. For each period, we have obtained group and phase velocities using the amplitude of wave group and phase of the wave, respectively. The resultant group velocity ranges between 2.9 km/s and 3.3 km/s. In Figure 20, we have shown one example of phase and group velocity dispersion curve. The predicted group and phase velocities are shown by black and blue lines, respectively. The group and phase velocities after corrections are indicated by blue triangles and orange squares respectively. The energy associated with this frequency-time diagram is shown using color contour. Here yellow color represents the higher value of energy and blue color represents the lower value. The best observed values of group/phase velocities have a higher value of energy. This means the group/phase velocity values residing in the yellow contour region gives us a more accurate estimation. Thus we have selected 3 sec to 14 sec period for plotting of group and phase velocity maps. The left side of Figure 20 is a basic FTAN measure and the right side is Phase-Matched FTAN measure. In basic FTAN measure, we didn't remove the noise from Green's functions which are used for computing group and phase velocities with respect to the period. This may cause error in precise estimation of dispersion curves. So to improve the quality of the dispersion curve, Phase-Matched FTAN [Levshin and Ritzwoller, 2001] is used. One of the vital use of this method is to improve the signal to noise ratio of the dispersion measurement. Total 4 steps are used in this method to obtain noise free dispersion curves:

1. Compute the dispersed signals using basic FTAN and compress them in time by applying
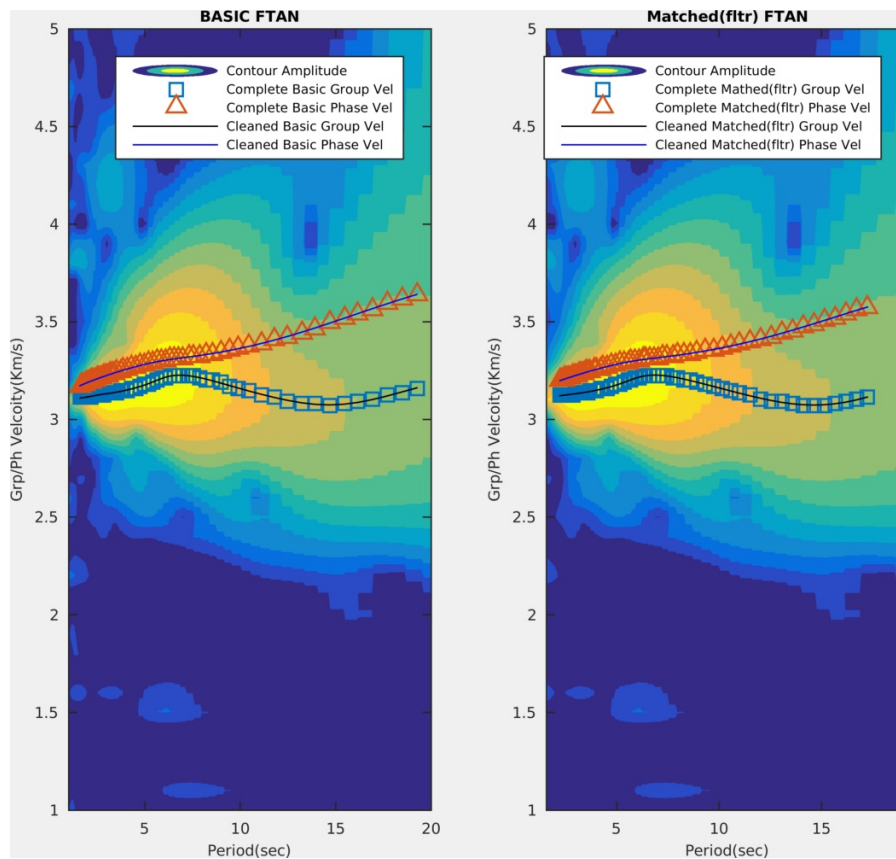
Figure 20 – Group and phase velocity dispersion curves obtained using FTAN: Group and phase velocities are shown by black (along with blue triangles) and blue lines (along with orange squares), respectively. Left: Basic FTAN dispersion curve. Right: Phase Matched filtered FTAN dispersion curve.

   an anti-dispersion or phase-matched filter. This signal is referred to as the *compressed signal*

2. Extract the Rayleigh wave by filtering the noise which is isolated from time-compressed signal.

3. Redispersed the filtered signal by applying inverse phase-matched filter on it and this will be filtered signal

4. Then the spectral amplitude and corrected group/phase velocities are measured

We have performed the group/phase velocity dispersion measurements only if the interstation spacing is three times the seismic wavelength for given period [Bensen et al., 2008]. After plotting the group/phase velocities, we have applied selection rule to extract useful dispersion curves:- Phase velocity is always greater than that of the group velocity and it is continuously increasing with the period. The dispersion curves which are not following this rule are discarded. Hence, we selected 60% of the total obtained dispersion curves for further analysis.

6.4 Group/Phase Velocity Maps

After computing the group/phase dispersion curves, we have calculated the traveltime between a virtual source and receiver using FMM (as described in section 4.2.2). We then computed both group and phase velocity maps using FMST (as described in sections 4.2.3 and 5.4). They are shown in Figure 21 and 22, respectively for the period range between 3 sec and 15 sec. For this, we have considered the initial velocity model as a constant velocity model. We have computed velocity maps for the period range between 3 sec and 15 sec with considering three factors, namely damping factor, smoothing factor and dicing factor. We kept damping factor as constant (equals to 1) and varied smoothing factor between 0 and 2. Smoothing factor equals to 0 means no smoothing. We kept 20 grid points for dicing level in latitude and longitude. The seismic wavelength was at least 3 times the minimum interstation spacing.

In Figure 21, we have considered the constant velocity background model (group velocity = 3.2 km/s), which is shown by red color in all the plots. In the region of East-West profile of South India, group velocity varies between 2.99 km/s to 3.15 km/s which signifies the less variation in group velocity. Although, the variation in velocity increases from period 4 sec to 8 sec and then starts steadily decreasing till 15 sec period.

In Figure 22, we again considered the constant velocity background model (phase velocity = 3.0 km/s), which is shown by green color in all plots. Here the phase velocity varies between 2.9 km/s and 3.05 km/s, which again show the less variation in group velocity. Here phase velocity didn't differ much with respect to the period, unlike group velocity.

In group and phase velocity dispersion curves or map, different period values denote the different depths. Here we obtained period range from 3 sec to 15 sec, which means roughly a depth from 10 km to 50 km. So this study lacks the information about shallow crustal part (less than 10 km). Also, variations in group velocity are more compared with in phase velocity. This tells us that the shallow crustal structure along the East-West profile is more sensitive to longer seismic wavelengths. Also, this less variation in phase velocity misses out the shallow crustal information at high-resolution scale (i.e., low wavelength).
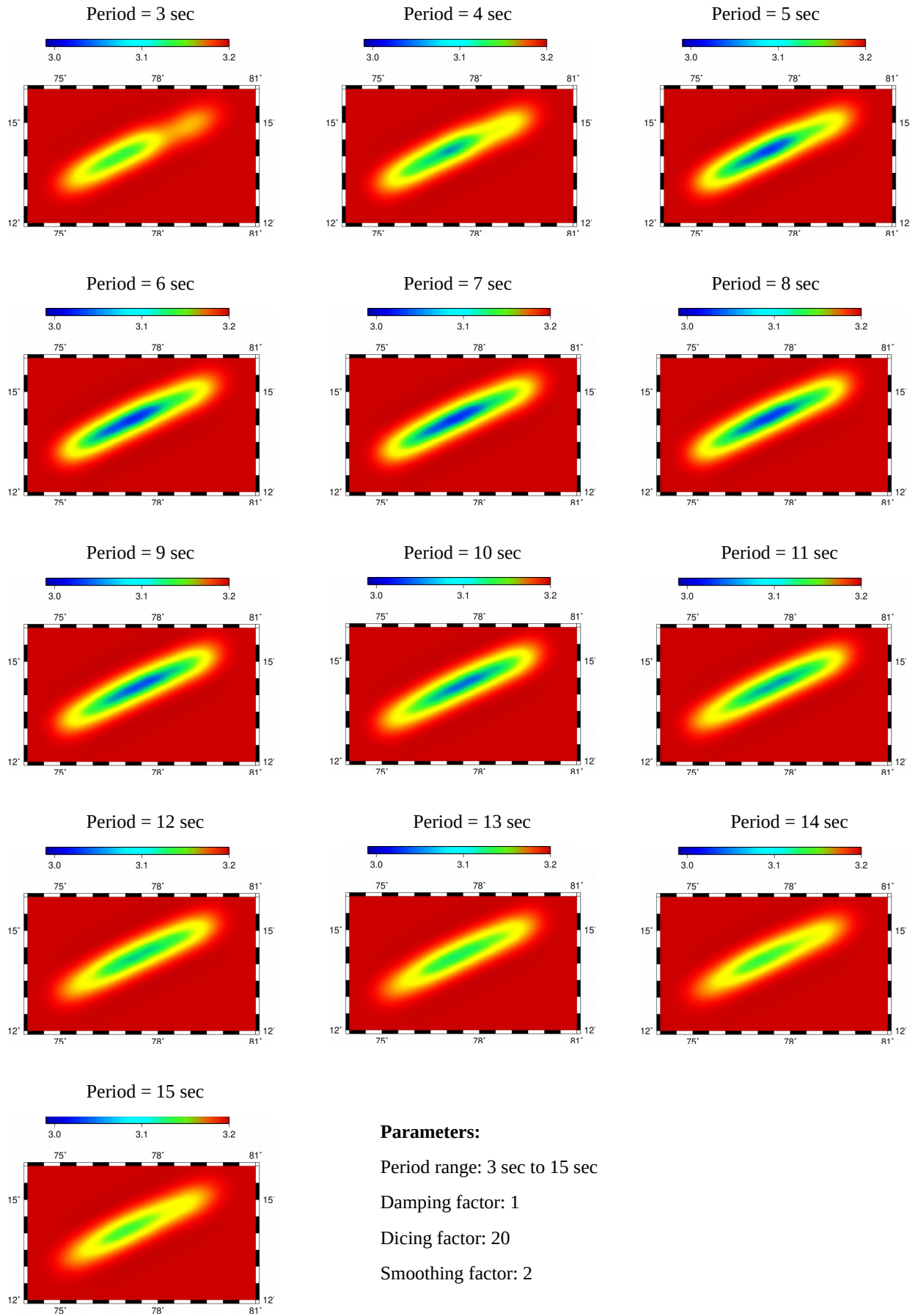
Figure 21 – Group velocity map for South India East-West profile for period range from 3 sec to 15 sec. The parameters for plotting these plots are mentioned in the bottom right of the figure
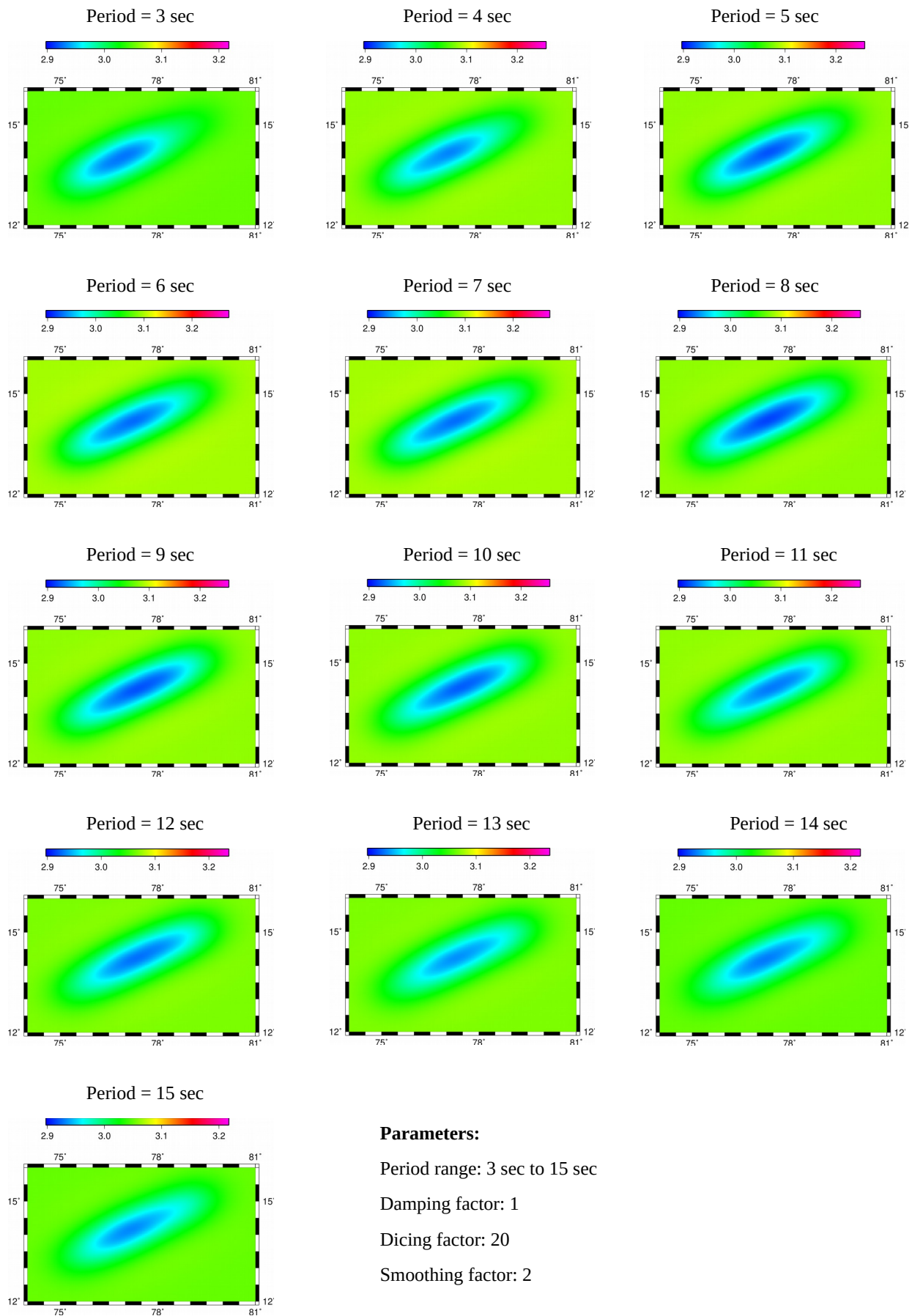
Figure 22 – Phase velocity map for South India East-West profile for period range from 3 sec to 15 sec. The parameters for plotting these plots are mentioned in the bottom right of the figure

7 Conclusion

The Rayleigh group and phase velocities at lower periods give us information about the shallow crustal part of the earth. In this study, we have obtained both the group and phase velocity maps using cross-correlations of the vertical component of ambient noise recorded on 38 broad-band seismometers along the East-West profile of South India. The cross-correlated functions were stacked to obtain Green's function between a virtual source and receiver. The group and phase velocity dispersion curves were obtained using Green's functions for the period range of 3 sec to 15 sec using basic and phase-matched FTAN. We then created the phase and group velocity maps for East-West profile of South India for given period range. In our study, we didn't get group and phase velocity dispersions below 3 sec period, which in turn lacks the information about the shallow crust. The variations in phase velocity were less compared with that of the group velocity, which was unable to generate the high resolution tomographic image of the East-West profile of South-India.

8 Future Prospective

We did not have obtained the actual tomographic image of East-West profile of South India to understand the seismic variations present in the shallow crust using group and phase velocity maps due to their low resolution content. The further step is to compute 1D shear wave velocity with to respect depth to understand the shear wave velocity profile in the shallow crust along the East-West profile of South India.

A Appendix: Seimograph Network

Details of broad-band seismograph network of South India East-West profile with period of operation

Sr.No	Stn Code	Lat (°N)	Long (°E)	Elav (m)	Sensor No.	Operational Period
1	SKL	13.016	74.833	40	CMG-3T	2012/05-2013/12
2	ALN	13.102	74.995	98	CMG-3T	2012/04-2013/12
3	STD	13.107	75.086	94	151B-120	2013/02-2013/12
4	HSR	13.134	75.120	100	151B-120	2013/02-2013/12
5	KMK	13.219	75.252	841	CMG-3T	2012/04-2013/12
6	BHL	13.268	75.430	805	CMG-3T	2012/04-2013/12
7	SPT	13.347	75.525	750	151B-120	2013/02-2013/12
8	BGS	13.407	75.616	996	CMG-3T	2012/04-2013/12
9	SVR	13.519	75.799	1260	CMG-3T	2012/04-2013/12
10	KDR	13.574	76.016	774	CMG-3T	2012/04-2013/12
11	KLR	13.690	76.175	706	CMG-3T	2012/04-2013/12
12	HSG	13.778	76.282	723	151B-120	2013/02-2013/12
13	MLR	13.864	76.400	668	CMG-3T	2012/04-2013/12
14	UDL	13.884	76.556	648	CMG-3T	2012/04-2013/12
15	DMR	13.987	76.719	589	CMG-3T	2012/04-2013/12
16	HYB	14.063	76.808	608	CMG-3T	2013/02-2013/12
17	AMR	14.077	76.942	605	CMG-3T	2012/04-2013/12
18	LDH	14.142	77.042	620	151B-120	2013/02-2014/01
19	PVG	14.180	77.102	694	CMG-3T	2012/04-2014/01
20	YSN	14.187	77.275	601	CMG-3T	2013/02-2014/01
21	PRR	14.294	77.352	570	CMG-3T	2012/04-2014/01
22	RMG	14.318	77.568	453	CMG-3T	2012/04-2014/01
23	MMP	14.414	77.645	390	CMG-3T	2013/02-2014/01
24	DMM	14.479	77.748	350	CMG-3T	2012/07-2014/01
25	BTP	14.522	77.840	321	151B-120	2013/02-2014/01
26	PRP	14.544	78.014	343	CMG-3T	2012/09-2014/01
27	SKS	14.653	78.209	245	CMG-3T	2012/09-2014/12
28	MDN	14.652	78.370	217	151B-120	2013/02-2014/01
29	RTP	14.734	78.471	171	CMG-3T	2012/09-2014/01
30	DUV	14.830	78.675	185	CMG-3T	2012/09-2014/01
31	PML	14.908	78.913	167	CMG-3T	2012/10-2014/01
32	RSP	14.980	79.016	105	151B-120	2013/02-2014/01
33	SRM	15.038	79.155	222	CMG-3T	2012/10-2014/01
34	PMR	15.100	79.371	123	CMG-3T	2009/05-2014/01
35	MPD	15.141	79.516	105	151B-120	2013/02-2014/01
36	IRD	15.174	79.599	108	CMG-3T	2012/10-2014/01
37	PNU	15.277	79.801	28	CMG-3T	2012/10-2014/01
38	KDL	15.425	79.996	16	CMG-3T	2013/10-2014/01

B   Appendix: Removing Poles and Zeros

The seismic trace or seismogram depends on the instrument response which is convloved with the ground motion and obtaining the actual ground motion requires the the removal of instrument response. This can be done by specifying the frequency response of the seismometer. This can be done by giving the amplitude and phase response of the instrument at each frequency. A more compact representation gives the frequency response as a complex fraction like

$$T(i\omega) = \frac{A \prod_{j=1}^{L}(i\omega - z_j)}{B \prod_{k=1}^{N}(i\omega - p_k)} \tag{76}$$

The fraction is described by a set of L complex zeros z_j at which the numerator is zero, N complex poles p_k at which the denominator is zero, and the constants are A and B . Because the frequency terms $i\omega$ are always imaginary and the poles always contain a real part, the denominator never becomes zero, avoiding any singular values. The poles and zeros are incorporated in the sensors of seismometer which are used to correct the instrument response and calibrated to its zero value.

References

Keiiti Aki and Paul G Richards. *Quantitative seismology*. 2002.

George B Arfken and Hans J Weber. Mathematical methods for physicists, 1999.

RD Beckinsale, SA Drury, and RW Holt. 3,360-myr old gneisses from the south indian craton. *Nature*, 283(5746):469, 1980.

GD Bensen, MH Ritzwoller, MP Barmin, AL Levshin, F Lin, MP Moschetti, NM Shapiro, and Yanyan Yang. Processing seismic ambient noise data to obtain reliable broad-band surface wave dispersion measurements. *Geophysical Journal International*, 169(3):1239–1260, 2007.

GD Bensen, MH Ritzwoller, and Nikolai M Shapiro. Broadband ambient noise surface wave tomography across the united states. *Journal of Geophysical Research: Solid Earth*, 113(B5), 2008.

Maurice A Biot. The interaction of rayleigh and stoneley waves in the ocean bottom. *Bulletin of the Seismological Society of America*, 42(1):81–93, 1952.

Kajaljyoti Borah, SS Rai, KS Prakasam, Sandeep Gupta, Keith Priestley, and VK Gaur. Seismic imaging of crust beneath the dharwar craton, india, from ambient noise and teleseismic receiver function modelling. *Geophysical Journal International*, 197(2):748–767, 2014.

Maud Boyet and Richard W Carlson. 142nd evidence for early (¿ 4.53 ga) global differentiation of the silicate earth. *Science*, 309(5734):576–581, 2005.

Ronald Newbold Bracewell and Ronald N Bracewell. *The Fourier transform and its applications*, volume 31999. McGraw-Hill New York, 1986.

Michel Campillo and Anne Paul. Long-range correlations in the diffuse seismic coda. *Science*, 299(5606):547–549, 2003.

B Chadwick, VN Vasudev, B Krishna Rao, and GV Hegde. The dharwar supergroup: Basin development and implications for late archaean tectonic setting in western karnataka, southern india. In *The Archaean: Terrains, Processes and Metallogeny*, volume 22, pages 3–15. University of Western Australia, 1992.

K Chandrakala, OP Pandey, ASSSRS Prasad, and K Sain. Seismic imaging across the eastern ghats belt-cuddapah basin collisional zone, southern indian shield and possible geodynamic implications. *Precambrian Research*, 271:56–64, 2015.

Nilanjan Chatterjee and Somdev Bhattacharji. Petrology, geochemistry and tectonic settings of the mafic dikes and sills associated with the evolution of the proterozoic cuddapah basin of south india. *Journal of Earth System Science*, 110(4):433–453, 2001.

K Roy Chowdhury and RB Hargraves. Deep seismic soundings in india and the origin of continental crust. *Nature*, 291(5817):648, 1981.

Jon F Claerbout. Synthesis of a layered medium from its acoustic transmission response. *Geophysics*, 33(2):264–269, 1968.

Andrew Curtis, Peter Gerstoft, Haruo Sato, Roel Snieder, and Kees Wapenaar. Seismic interferometryâturning noise into signal. *The Leading Edge*, 25(9):1082–1092, 2006.

Sukanta Dey. Evolution of archaean crust in the dharwar craton: the nd isotope record. *Precambrian Research*, 227:227–246, 2013.

Thomas L Duvall Jr, SM Jeffferies, JW Harvey, and MA Pomerantz. Time–distance helioseismology. *Nature*, 362(6419):430, 1993.

A Dziewonski. A technique for the analysis of transient seismic signals. *Bull. Seism. Soc. Am*, 61:343–356, 1971.

Adam M Dziewonski and Don L Anderson. Preliminary reference earth model. *Physics of the earth and planetary interiors*, 25(4):297–356, 1981.

Berenice Froment, Michel Campillo, Philippe Roux, Pierre Gouedard, Arie Verdel, and Richard L Weaver. Estimation of the effect of nonisotropically distributed energy on the apparent arrival time in correlations. *Geophysics*, 75(5):SA85–SA93, 2010.

Josselin Garnier and George Papanicolaou. Passive sensor imaging using cross correlations of noisy signals in a scattering medium. *SIAM Journal on Imaging Sciences*, 2(2):396–437, 2009.

PAUL Goldstein and A Snoke. Sac availability for the iris community. *Incorporated Research Institutions for Seismology Newsletter*, 7(UCRL-JRNL-211140), 2005.

Pierre Gouedard, L Stehly, F Brenguier, Michel Campillo, Y Colin De Verdière, Eric Larose, L Margerin, P Roux, Francisco J Sánchez-Sesma, NM Shapiro, et al. Cross-correlation of random fields: mathematical approach and applications. *Geophysical prospecting*, 56(3): 375–393, 2008.

George Green. An essay on the application of mathematical analysis to the theories of electricity and magnetism. *Journal für die reine und angewandte Mathematik*, 47:161–221, 1854.

David Gubbins. *Time series analysis and inverse theory for geophysicists*. Cambridge University Press, 2004.

Yanni Gunnell and BP Radhakrishna. *Sahyādri: The Great Escarpment of the Indian Subcontinent: Patterns of Landscape Development in the Western Ghats*. Geological Society of India, 2001.

K Hasselmann. A statistical analysis of the generation of microseisms. *Reviews of Geophysics*, 1(2):177–210, 1963.

Eugene Herrin and Tom Goforth. Phase-matched filters: application to the study of rayleigh waves. *Bulletin of the Seismological Society of America*, 67(5):1259–1275, 1977.

Gregor Hillers, Nicholas Graham, Michel Campillo, S Kedar, Matthieu Landès, and N Shapiro. Global oceanic microseism sources as seen by seismic arrays and predicted by wave action models. *Geochemistry, Geophysics, Geosystems*, 13(1), 2012.

KL Kaila, K Roy Chowdhury, PR Reddy, VG Krishna, Hari Narain, SI Subbotin, VB Sollogub, AV Chekunov, GE Kharetchko, MA Lazarenko, et al. Crustal structure along kavali-udipi profile in the indian peninsular shield from deep seismic sounding. *J. Geol. Soc. India*, 20 (7):307–333, 1979.

Keith D Koper, Benjamin de Foy, and Harley Benz. Composition and variation of noise recorded at the yellowknife seismic array, 1991–2007. *Journal of Geophysical Research: Solid Earth*, 114(B10), 2009.

Matthieu Landès, Fabien Hubans, Nikolai M Shapiro, Anne Paul, and Michel Campillo. Origin of deep ocean microseisms by using teleseismic body waves. *Journal of Geophysical Research: Solid Earth*, 115(B5), 2010.

Eric Larose, Arnaud Derode, Michel Campillo, and Mathias Fink. Imaging from one-bit correlations of wideband diffuse wave fields. *Journal of Applied Physics*, 95(12):8393–8399, 2004.

AL Levshin and MH Ritzwoller. Automated detection, extraction, and measurement of regional surface waves. In *Monitoring the Comprehensive Nuclear-Test-Ban Treaty: Surface Waves*, pages 1531–1545. Springer, 2001.

Anatoli Levshin, Ludmila Ratnikova, and JON Berger. Peculiarities of surface-wave propagation across central eurasia. *Bulletin of the Seismological Society of America*, 82(6):2464–2493, 1992.

Anatoli L Levshin, VF Pisarenko, and GA Pogrebinsky. On a frequency-time analysis of oscillations. In *Annales de Geophysique*, volume 28, pages 211–218. Centre National de la Recherche Scientifique, 1972.

Fan-Chi Lin, Morgan P Moschetti, and Michael H Ritzwoller. Surface wave tomography of the western united states from ambient seismic noise: Rayleigh and love wave phase velocity maps. *Geophysical Journal International*, 173(1):281–298, 2008.

Guochang Liu, Sergey Fomel, Long Jin, and Xiaohong Chen. Stacking seismic data using local correlation. *Geophysics*, 74(3):V43–V48, 2009.

Oleg I Lobkis and Richard L Weaver. On the emergence of the green's function in the correlations of a diffuse field. *The Journal of the Acoustical Society of America*, 110(6):3011–3017, 2001.

Michael Selwyn Longuet-Higgins. A theory of the origin of microseisms. *Philosophical Transactions of the Royal Society of London. Series A, Mathematical and Physical Sciences*, 243 (857):1–35, 1950.

Michael Selwyn Longuet-Higgins. The directional spectrum of ocean waves, and processes of wave generation. *Proceedings of the Royal Society of London. Series A. Mathematical and Physical Sciences*, 265(1322):286–315, 1962.

DM Mall, K Chandrakala, A Sudhir Kumar, and D Sarkar. Sub-crustal lvz below dharwar craton, india: an evidence for mantle metasomatism and tectonothermal activity in the archean crust. *Precambrian Research*, 208:161–173, 2012.

James K Meen, John JW Rogers, and Paul D Fullagar. Lead isotopic compositions of the western dharwar craton, southern india: evidence for distinct middle archean terranes in a late archean craton. *Geochimica et Cosmochimica Acta*, 56(6):2455–2470, 1992.

Joseph G Meert, Manoj K Pandit, Vimal R Pradhan, Jonathan Banks, Robert Sirianni, Misty Stroud, Brittany Newstead, and Jennifer Gifford. Precambrian crustal evolution of peninsular india: a 3.0 billion year odyssey. *Journal of Asian Earth Sciences*, 39(6):483–515, 2010.

William Menke. *Geophysical data analysis: Discrete inverse theory*. Academic press, 2018.

Albert A Michelson and Edward W Morley. On the relative motion of the earth and of the luminiferous ether. *Sidereal Messenger, vol. 6, pp. 306-310*, 6:306–310, 1887.

MP Moschetti, MH Ritzwoller, and NM Shapiro. Surface wave tomography of the western united states from ambient seismic noise: Rayleigh wave group velocity maps. *Geochemistry, Geophysics, Geosystems*, 8(8), 2007.

S Mahmood Naqvi and John James William Rogers. *Precambrian geology of India*. Oxford University Press, 1987.

IO Norton and JG Sclater. A model for the evolution of the indian ocean and the breakup of gondwanaland. *Journal of Geophysical Research: Solid Earth*, 84(B12):6803–6830, 1979.

CD Ollier and KB Powar. *The Western Ghats and the morphotectonics of peninsular India*. 1985.

M PA. Physical interpretation of quantum mechanics. *Nature*, 148:28, 1941.

Robert L Parker and Robert L Parker. *Geophysical inverse theory*. Princeton university press, 1994.

Charles S Pichamuthu and R Srinivasan. *The Dharwar Craton*, volume 7. Indian National Science Academy, 1984.

Alexander Mihai Popovici and James A Sethian. 3-d imaging using higher order fast marching traveltimes. *Geophysics*, 67(2):604–609, 2002.

John G Proakis. *Digital signal processing: principles algorithms and applications*. Pearson Education India, 2001.

M Ravi Kumar and Arun Singh. Seismic anisotropy of the indian tectonic plate: deciphering continental scale mantle deformation patterns. *Current Science (00113891)*, 99(12), 2010.

Nicholas Rawlinson and Malcolm Sambridge. Wave front evolution in strongly heterogeneous layered media using the fast marching method. *Geophysical Journal International*, 156(3): 631–647, 2004a.

Nicholas Rawlinson, Malcolm Sambridge, et al. Seismic traveltime tomography of the crust and lithosphere. *Advances in Geophysics*, 46:81–199, 2003.

Nick Rawlinson and Malcolm Sambridge. Multiple reflection and transmission phases in complex layered media using a multistage fast marching method. *Geophysics*, 69(5):1338–1350, 2004b.

James Rickett and Jon Claerbout. Acoustic daylight imaging via spectral factorization: Helioseismology and reservoir monitoring. *The leading edge*, 18(8):957–960, 1999.

Michael H Ritzwoller and Anatoli L Levshin. Eurasian surface wave tomography: Group velocities. *Journal of Geophysical Research: Solid Earth*, 103(B3):4839–4878, 1998.

Philippe Roux, WA Kuperman, and NPAL Group. Extracting coherent wave fronts from acoustic ambient noise in the ocean. *The Journal of the Acoustical Society of America*, 116 (4):1995–2003, 2004.

Philippe Roux, Karim G Sabra, Peter Gerstoft, WA Kuperman, and Michael C Fehler. P-waves from cross-correlation of seismic noise. *Geophysical Research Letters*, 32(19), 2005a.

Philippe Roux, Karim G Sabra, William A Kuperman, and Andre Roux. Ambient noise cross correlation in free space: Theoretical approach. *The Journal of the Acoustical Society of America*, 117(1):79–84, 2005b.

David R Russell, Robert B Herrmann, and Horng-Jye Hwang. Application of frequency variable filters to surface-wave amplitude analysis. *Bulletin of the Seismological Society of America*, 78(1):339–354, 1988.

Karim G Sabra, Peter Gerstoft, Philippe Roux, WA Kuperman, and Michael C Fehler. Extracting time-domain green's function estimates from ambient seismic noise. *Geophysical Research Letters*, 32(3), 2005a.

Karim G Sabra, Peter Gerstoft, Philippe Roux, WA Kuperman, and Michael C Fehler. Surface wave tomography from microseisms in southern california. *Geophysical Research Letters*, 32 (14), 2005b.

Utpal Saikia, SS Rai, Rishikesh Meena, BNV Prasad, and Kajaljyoti Borah. Moho offsets beneath the western ghat and the contact of archean crusts of dharwar craton, india. *Tectonophysics*, 672:177–189, 2016.

Utpal Saikia, Ritima Das, and SS Rai. Possible magmatic underplating beneath the west coast of india and adjoining dharwar craton: Imprint from archean crustal evolution to breakup of india and madagascar. *Earth and Planetary Science Letters*, 462:1–14, 2017.

Martin Schimmel. Phase cross-correlations: Design, comparisons, and applications. *Bulletin of the Seismological Society of America*, 89(5):1366–1378, 1999.

Martin Schimmel and Hanneke Paulssen. Noise reduction and detection of weak, coherent signals through phase-weighted stacks. *Geophysical Journal International*, 130(2):497–505, 1997.

JG Scholte. The range of existence of rayleigh and stoneley waves. *Geophysical Supplements to the Monthly Notices of the Royal Astronomical Society*, 5(5):120–126, 1947.

Gerard T Schuster and Roel Snieder. Seismic interferometry. *Acoustical Society of America Journal*, 126:3375, 2009.

James A Sethian. A fast marching level set method for monotonically advancing fronts. *Proceedings of the National Academy of Sciences*, 93(4):1591–1595, 1996.

James A Sethian and A Mihai Popovici. 3-d traveltime computation using the fast marching method. *Geophysics*, 64(2):516–523, 1999.

James Albert Sethian. *Level set methods and fast marching methods: evolving interfaces in computational geometry, fluid mechanics, computer vision, and materials science*, volume 3. Cambridge university press, 1999.

Nikolai M Shapiro and Michel Campillo. Emergence of broadband rayleigh waves from correlations of the ambient seismic noise. *Geophysical Research Letters*, 31(7), 2004.

Nikolai M Shapiro, Michael H Ritzwoller, Peter Molnar, and Vadim Levin. Thinning and flow of tibetan crust constrained by seismic anisotropy. *Science*, 305(5681):233–236, 2004.

Nikolai M Shapiro, Michel Campillo, Laurent Stehly, and Michael H Ritzwoller. High-resolution surface-wave tomography from ambient seismic noise. *Science*, 307(5715):1615–1618, 2005.

NM Shapiro and MH Ritzwoller. Monte-carlo inversion for a global shear-velocity model of the crust and upper mantle. *Geophysical Journal International*, 151(1):88–105, 2002.

George F Simmons. *Differential equations with applications and historical notes*. CRC Press, 2016.

Roel Snieder. Extracting the greenâs function from the correlation of coda waves: A derivation based on stationary phase. *Physical Review E*, 69(4):046610, 2004.

Roel Snieder. The theory of coda wave interferometry. *Pure and Applied geophysics*, 163(2-3): 455–473, 2006.

Ivan Stephen Sokolnikoff, Robert Dickerson Specht, et al. *Mathematical theory of elasticity*, volume 83. McGraw-Hill New York, 1956.

L Stehly, B Fry, Michel Campillo, NM Shapiro, J Guilbert, L Boschi, and D Giardini. Tomography of the alpine region from observations of seismic ambient noise. *Geophysical Journal International*, 178(1):338–350, 2009.

Holly J Stein, Judith L Hannah, Aaron Zimmerman, Richard J Markey, Sanjib C Sarkar, and AB Pal. A 2.5 ga porphyry cu–mo–au deposit at malanjkhand, central india: implications for late archean continental assembly. *Precambrian Research*, 134(3-4):189–226, 2004.

Seth Stein and Michael Wysession. *An introduction to seismology, earthquakes, and earth structure*. John Wiley & Sons, 2009.

Robert Glenn Stockwell, Lalu Mansinha, and RP Lowe. Localization of the complex spectrum: the s transform. *IEEE transactions on signal processing*, 44(4):998–1001, 1996.

Michael Storey, John J Mahoney, Andrew D Saunders, Robert A Duncan, Simon P Kelley, and Millard F Coffin. Timing of hot spotârelated volcanism and the breakup of madagascar and india. *Science*, 267(5199):852–855, 1995.

John William Strutt. On waves propagated along the plane surface of an elastic solid. *Proceedings of the London Mathematical Society*, 17(1):4–11, 1885.

E Stutzmann, F Ardhuin, Martin Schimmel, A Mangeney, and G Patau. Modelling long-term seismic noise in various environments. *Geophysical Journal International*, 191(2):707–722, 2012.

Eléonore Stutzmann, Jean-Paul Montagner, Amal Sebai, Wayne C Crawford, Jean-Louis Thirot, Pascal Tarits, Debra Stakes, Barbara Romanowicz, Jean-Francois Karczewski, Jean-Claude Koenig, et al. Moise: a prototype multiparameter ocean-bottom station. *Bulletin of the Seismological Society of America*, 91(4):885–892, 2001.

Eleonore Stutzmann, Martin Schimmel, Genevieve Patau, and Alessia Maggi. Global climate imprint on seismic noise. *Geochemistry, Geophysics, Geosystems*, 10(11), 2009.

T Tanimoto, S Ishimaru, and C Alvizuri. Seasonality in particle motion of microseisms. *Geophysical Journal International*, 166(1):253–266, 2006.

A Tarantola. Inverse problem theory elsevier. *New York*, 1987.

PN Taylor, B Chadwick, S Moorbath, M Ramakrishnan, and MN Viswanatha. Petrography, chemistry and isotopic ages of peninsular gneiss, dharwar acid volcanic rocks and the chitradurga granite with special reference to the late archean evolution of the karnataka craton, southern india. *Precambrian Research*, 23(3-4):349–375, 1984.

CJ Thomson and D Gubbins. Three-dimensional lithospheric modelling at norsar: linearity of the method and amplitude variations from the anomalies. *Geophysical Journal International*, 71(1):1–36, 1982.

Sergi Ventosa, Martin Schimmel, and Eleonore Stutzmann. Extracting surface waves, hum and normal modes: time-scale phase-weighted stack and beyond. *Geophysical Journal International*, 211(1):30–44, 2017.

Kees Wapenaar. Synthesis of an inhomogeneous medium from its acoustic transmission response. *Geophysics*, 68(5):1756–1759, 2003.

Kees Wapenaar. Retrieving the elastodynamic green's function of an arbitrary inhomogeneous medium by cross correlation. *Physical review letters*, 93(25):254301, 2004.

Kees Wapenaar and Jacob Fokkema. Greenâs function representations for seismic interferometry. *Geophysics*, 71(4):SI33–SI46, 2006.

Kees Wapenaar, Deyan Draganov, Roel Snieder, Xander Campman, and Arie Verdel. Tutorial on seismic interferometry: Part 1âbasic principles and applications. *Geophysics*, 75(5): 75A195–75A209, 2010a.

Kees Wapenaar, Evert Slob, Roel Snieder, and Andrew Curtis. Tutorial on seismic interferometry: Part 2âunderlying theory and new advances. *Geophysics*, 75(5):75A211–75A227, 2010b.

Richard Weaver, Berenice Froment, and Michel Campillo. On the correlation of non-isotropically distributed ballistic scalar diffuse waves. *The Journal of the Acoustical Society of America*, 126(4):1817–1826, 2009.

Richard L Weaver and Oleg I Lobkis. Ultrasonics without a source: Thermal fluctuation correlations at mhz frequencies. *Physical Review Letters*, 87(13):134301, 2001.

Richard L Weaver and Oleg I Lobkis. Fluctuations in diffuse field–field correlations and the emergence of the greenâs function in open systems. *The Journal of the Acoustical Society of America*, 117(6):3432–3439, 2005.

Paul Wessel, Walter HF Smith, Remko Scharroo, Joaquim Luis, and Florian Wobbe. Generic mapping tools: improved version released. *Eos, Transactions American Geophysical Union*, 94(45):409–410, 2013.

Jiayi Xie, Michael H Ritzwoller, SJ Brownlee, and BR Hacker. Inferring the oriented elastic tensor from surface wave observations: preliminary application across the western united states. *Geophysical Journal International*, 201(2):996–1021, 2015.

Yingjie Yang, Michael H Ritzwoller, Anatoli L Levshin, and Nikolai M Shapiro. Ambient noise rayleigh wave tomography across europe. *Geophysical Journal International*, 168(1):259–274, 2007.

T Yanovskaya, AL Levshin, EN Its, AV Lander, BG Bukchin, MP Barmin, and LI Ratnikova. *Seismic surface waves in a laterally inhomogeneous Earth*, volume 9. Springer Science & Business Media, 2012.

Huajian Yao, Xander Campman, V Maarten, and Robert D van der Hilst. Estimation of surface wave green's functions from correlation of direct waves, coda waves, and ambient noise in se tibet. *Physics of the Earth and Planetary Interiors*, 177(1-2):1–11, 2009.

MK Young, Nicholas Rawlinson, Pierre Arroucau, Anya M Reading, and H Tkalčić. High-frequency ambient noise tomography of southeast australia: New constraints on tasmania's tectonic past. *Geophysical Research Letters*, 38(13), 2011.